

Supporting Information

Ferro- or Antiferromagnetism? Heisenberg Chains in the Crystal Structures of Verdazyl Radicals

Steffen Eusterwiemann,^a Carsten Doerenkamp,^b Thomas Dresselhaus,^{a,c} Oliver Janka,^d Constantin G. Daniliuc,^a Rainer Pöttgen,^{d*} Armido Studer,^{a*} Hellmut Eckert,^{b,e*} and Johannes Neugebauer^{a,c*}

^a Organisch-Chemisches Institut, Westfälische Wilhelms-Universität Münster, Corrensstrasse 40, 48149 Münster, Germany

^b Institut für Physikalische Chemie, Westfälische Wilhelms-Universität Münster, Corrensstrasse 28/30, 48149 Münster, Germany

^c Center for Multiscale Theory and Computation, Westfälische Wilhelms-Universität Münster, Corrensstrasse 40, 48149 Münster, Germany

^d Institut für Anorganische und Analytische Chemie, Westfälische Wilhelms-Universität Münster, Corrensstrasse 28/30, 48149 Münster, Germany

^e Instituto da Física em Sao Carlos, Universidade de Sao Paulo, Avenida Trabalhador Saocarlene 400, Sao Carlos, São Paulo 13566-590, Brazil

* E-mail: pottgen@uni-muenster.de (R.P.), studer@uni-muenster.de (A.S.), eckerth@uni-muenster.de (H.E.), j.neugebauer@uni-muenster.de (J.N.)

Table of content

1 General Methods and Information	3
2 Experimental Section	5
General Procedures	5
Preparation of Precursor Compounds	5
Preparation of Verdazyl Radicals.....	6
3 X-Ray Crystal Structure Analysis	9
X-ray Crystal Structure Analysis of 3	9
X-ray Crystal Structure Analysis of 4	11
X-ray Crystal Structure Analysis of 5 and Discussion of Magnetic Topology.....	13
X-ray Crystal Structure Analysis of 6	16
4 EPR Spectroscopy.....	19
5 Physical Properties	20
6 Theoretical Calculations	24
7 UV/Vis Absorption Spectroscopy.....	31
8 Cyclic Voltammetry Measurements	33
9 ^1H and ^{13}C NMR Spectra.....	34
10 References.....	36

1 General Methods and Information

¹H NMR- and ¹³C NMR spectra were recorded with a *DPX-300* (¹H: 300 MHz; ¹³C: 75 MHz) from *Bruker* at 298–300 K. The signals of the solvents were calibrated upon CDCl₃ and DMSO-*d*₆ in ¹H NMR- spectra to the literature known value at δ 7.260 ppm and 3.330 ppm, in ¹³C NMR spectra relative to deuterated signal at δ 77.160, 39.520 ppm.¹ The coupling constants *J* are given in Hz. The chemical shift in ppm are given relative to the resonance signal of the internal standard tetramethylsilane (δ 0.00 ppm). Spectral splitting pattern are designated as *s* (singlet), *d* (doublet), *t* (triplet), *m* (multiplet) and *br* (broad signal). **Mass spectra** (HRMS–ESI) were recorded on a *Finnigan MAT 4200S* and a *Bruker Daltonics Micro-TOF*. **IR spectra** were recorded on a *Varian associates FT-IR 3100* equipped with a MKII Golden Gate Single Reflection ATR unit. Recorded IR signals are reported as wavelength (cm⁻¹) with the following abbreviation for the intensity of absorption: *s* = strong, *m* = medium, *w* = weak. **Melting points** (M.p.) (uncorrected) were measured on a *Stuart SMP-10* melting point apparatus. **Elemental analysis** were performed at a *Vario EL III* of the company *Elementar-Analysensysteme GmbH*, Hanau. **UV/Vis absorption spectroscopy** measurements were performed at rt in CH₂Cl₂ (~ 0.83 mM) in a quartz glass cuvette (0.1 mm QS) with a *Varian Cary 1Bio*. **EPR** spectra were recorded with a *Bruker E-580 ELEXIS EPR spectrometer* (9.4 GHz, X-Band, magnetic field of 0.34 T). A 0.5 mM radical solution in deoxygenated toluene (at RT) and solid radicals (at 50 K) were measured in thin Borosilicate EPR tubes. The modulation amplitude was set between 0.5 and 1.0 Gauss at a modulation frequency of 100 kHz. Typically, 1024 data points per spectrum at a center field of 337.5 mT and a sweep width of 10 to 15 mT with a sweep-time between 83.89 and 167.77 s were used. The calibration of the *g*-values was done with the DHHP standard (*g* = 2.0036). The data were analyzed and simulated with MatLab and EasySpin 5.2.11. **Thin layer chromatography (TLC)** was carried out on Merck silica gel 60 F254 plates; detection by UV (irradiation at 254 nm) or dipping into a solution of KMnO₄ (1.5 g), NaHCO₃ (5.0 g) in H₂O (400 mL), followed by heating. **Flash chromatography (FC)** was performed on silica gel (*Merck-Si60* 40–63 μ m) with a pressure of 0.1–0.5 bar. Used eluents are given in parentheses. **Medium Pressure Liquid Chromatography (MPLC)** was performed on a *Grace Davison Reveleris IES Flash Chromatography System* with *Reveleris Amino* cartridges (4.0 g) at a flow rate of 14 mL/min and with cyclohexane, EtOAc, CH₂Cl₂ and MeOH as solvents (UV detection (254 nm) and ELSD-detection with *iso*-propanol as ELSD carrier). **Cyclic voltammetry measurements** were performed in an undivided microcell (5 mL, *Metrohm*) with Ag/AgCl-reference electrode (0.1 M Bu₄NBF₄ in MeCN; + 0.21 V vs. SHE), with a glassy carbon as counter electrode and under a cyclic platinum electrode (*d* = 3 mm) as

working electrode. As an internal standard ferrocene was added after each measurement and the redox potential of it set to 0 V. The current flow was applied with a *potentiostat PG-STAT 20* in combination with a *VA 663 (Metrohm)*. A scan rate of 0.1 V s^{-1} was used for the measurements. The analysis software *GPES 4.6 (Eco-Chemie B.V.)* was applied for analysis. **Solvents and reagents:** All solvents for extraction and flash chromatography (FC) were distilled before use. Et_2O was distilled from K/Na and CH_2Cl_2 was distilled from P_2O_5 . All other solvents and reagents were purchased of the following companies and have been used without further purification: *Acros Organics, Sigma-Aldrich, Alfa Aesar, TCI Germany* or *Merck*. The oxidizing agent DMP (Dess Martin periodinane)² and the precursor compounds 2,4-diphenylcarbonohydrazide (**1**)³, 5-(trimethylsilyl)penta-2,4-diyne-1-ol⁴, 4-ethynylbenzaldehyde⁵ and 4-((trimethylsilyl)ethynyl)benzaldehyde⁵ were synthesized in accordance to procedures reported earlier. **Techniques:** All glasswares were dried by the use of a heat gun under high vacuum prior to use. Concentration of the reaction mixture was performed under reduced pressure at $40 \text{ }^\circ\text{C}$ at the appropriate pressure. Purified compounds were further dried under high vacuum.

2 Experimental Section

General Procedures

GP1: Synthesis of tetrazinan-3-ones

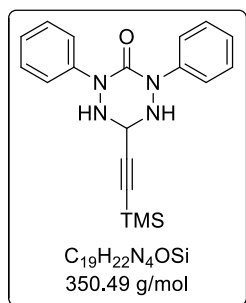
In a two necked round bottom flask with condenser 2,4-diphenylcarbonohydrazide (**1**) (1.0 eq.) was dissolved in MeOH. A solution of the aldehyde (1.0 eq.) in MeOH was added with a syringe-pump within 30 min at 40 °C. Then the temperature was raised to 60 °C for 3 h. After cooling down to rt a precipitate was filtered off to afford the tetrazinan-3-one as a colorless solid, which was dried *in vacuo*.

GP2: Oxidation of tetrazinan-3-ones to verdazyl radicals

In a sealed tube tetrazinan-3-one (1.0 eq.) was dissolved in CH₂Cl₂ and 1,4-benzoquinone (≥1.5 eq.) was added. The solution was heated for 3–4 h at 60 °C After the reaction mixture was allowed to cool to rt the solvent was removed *in vacuo* and the residue subjected to FC, which afforded the verdazyl radical.

Preparation of Precursor Compounds

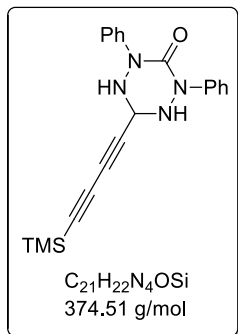
1,5-Dihydro-2,4-Diphenyl-6-trimethylsilylethynyl-1,2,4,5-tetrazinan-3(2H)-one (**2**)



According to **GP1** with 3-trimethylsilylpropynal (0.16 mL, 1.26 mmol, 1.0 eq.) and 2,4-diphenylcarbonohydrazide (1.31 g, 1.26 mmol, 1.0 eq.). Filtration afforded the title compound (0.30 g, 0.86 mmol, 68%) as a colorless solid. **M.p.**: 181 °C (decomp.); **IR** (ATR, neat): 3260w, 3196w, 2964w, 1685m, 1624s, 1596m, 1495m, 1454m, 1377s, 1345m, 1298m, 1251s, 1172w, 1110w, 1074w, 1028m, 970w, 918s, 888m, 835s, 755s, 723m, 689s, 650w, 621m, 609m, 577w, 554m, 525m; **¹H NMR** (300 MHz,

CDCl₃): δ 7.62 (dd, *J* = 8.7, 1.1 Hz, 4H, CH_{arom}), 7.36 – 7.29 (m, 4H, CH_{arom}), 7.13 (t, *J* = 7.4 Hz, 2H, CH_{arom}), 5.05 (m, 1H, NCHN), 4.83 (d, *J* = 8.6 Hz, 2H, NH), 0.17 (s, 9H, CH₃); **¹³C NMR** (75 MHz, CDCl₃): δ 154.8 (C), 142.2 (C), 128.5 (CH), 125.0 (CH), 122.6 (CH), 98.3 (C), 92.9 (C), 63.5 (CH), -0.3 (CH₃); **HRMS** (ESI): *m/z* = 373.1455, 723.3018 calcd. for [M+Na]⁺, [2M+Na]⁺, found: 373.1462, 723.3012.

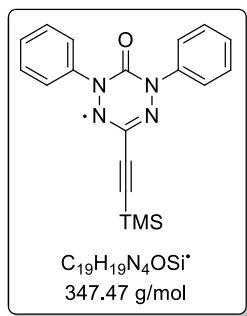
2,4-Diphenyl-6-((trimethylsilyl)buta-1,3-diyne-1-yl)-1,2,4,5-tetrazinan-3-one (2b)



In accordance to a literature procedure from BOWLING *et al.*⁴ Dess Martin periodinane (966 mg, 2.28 mmol, 1.4 Äq.) was added to a solution of 5-(trimethylsilyl)penta-2,4-diyne-1-ol (248 mg, 1.63 mmol, 1.0 Äq.) in CH_2Cl_2 (13 mL) and the mixture was stirred at rt for 1.5 h. Then Et_2O (10 mL) was added and the suspension filtered over *Celite*. The solvents were removed *in vacuo* and the residue subjected to a column filtration (*n*-pentane/MTBE 8:1). After concentration of the filtrate to a volume of around 2 mL, the yield of the aldehyde (5-(trimethylsilyl)penta-2,4-diyнал, 1.04 mmol, 63%) was determined by 1H NMR spectroscopy using an internal standard (CH_2Br_2). The residue was diluted with MeOH (1 mL), which was added dropwise within 30 min to a solution of 2,4-diphenylcarbonohydrazide (251 mg, 1.04 mmol, 1.0 eq.) in MeOH (4 mL) at 40 °C. After the reaction mixture was stirred at 60 °C for 2.5 h, the resulting precipitate was filtered off and washed carefully with cold MeOH. A further drying *in vacuo* afforded the title compound (267 mg, 713 μ mol, 69%, total yield over two steps: 43%) as a colorless solid. R_F : 0.21 (*n*-pentane/MTBE 2:1); **M.p.**: 205 °C (decomp.); **IR** (ATR, neat): 3258w, 2110w, 1625m, 1492w, 1364s, 1327w, 1250w, 1175w, 1069w, 914m, 846s, 756s, 689m, 609w; **1H NMR** (300 MHz, $DMSO-d_6$): δ 7.53 (dd, $J = 8.7, 1.3$ Hz, 4H, CH_{arom}), 7.33 (dd, $J = 8.6, 7.2$ Hz, 4H, CH_{arom}), 7.09 (t, $J = 7.3$ Hz, 2H, CH_{arom}), 6.58 (d, $J = 6.2$ Hz, 2H, NH), 5.35 (t, $J = 6.2$ Hz, 1H, CH), 0.17 (s, 9H, CH_3); **^{13}C NMR** (101 MHz, $DMSO-d_6$): δ 155.2 (C), 142.8 (C), 128.3 (CH), 124.2 (CH), 122.2 (CH), 88.4 (C), 87.2 (C), 74.7 (C), 68.5 (C), 62.1 (CH), -0.5 (CH_3); **HRMS** (ESI): $m/z = 375.1636, 397.1455$ cacl. for $[M+H]^+$, found: 375.1649, 397.1468.

Preparation of Verdazyl Radicals

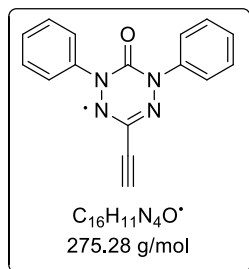
1,5-Diphenyl-3-trimethylsilylethynyl-6-oxo-verdazyl (3)



According to **GP2** with tetrazinan-3-one **2** (0.10 g, 0.28 mmol, 1.0 eq) and 1,4-benzoquinone (0.14 g, 1.25 mmol, 4.4 eq.). FC (*n*-pentane/MTBE 12:1) afforded the title compound (0.10 g, 0.28 mmol, 98%) as a dark red solid. Crystals suitable for single crystal X-Ray crystallography were obtained by slow evaporation of a $CHCl_3$ solution of the sample at rt. R_F : 0.34; **M.p.**: 163 °C; **IR** (neat): 3068w, 2963w, 1742w, 1704m, 1593w, 1485w, 1459w, 1390w, 1357w, 1297m, 1222s, 1180s, 1127s, 1027w, 982s, 925w, 846s,

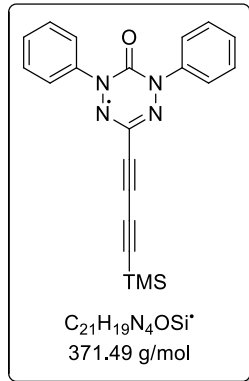
756s, 711m, 690s, 679s, 656s, 602s, 509s; **HRMS** (ESI): $m/z = 370.1220, 717.2548$ calcd. for $[M+Na]^+$, $[2M+Na]^+$; found: 370.1224, 717.2542; **Anal. Calcd.** for $C_{19}H_{19}N_4OSi$, C: 69.81, H: 4.03, N: 20.35; found: 69.58, 4.23, 19.97.

1,5-Diphenyl-3-ethynyl-6-oxo-verdazyl (4)



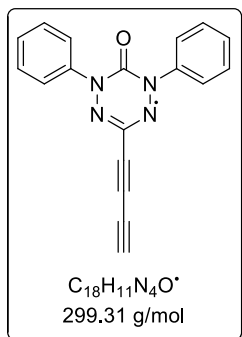
In a round bottom flask verdazyl radical **3** (0.13 g, 0.36 mmol, 1.0 eq.) was dissolved in acetone (20 mL) and KF (0.20 g, 3.45 mmol, 9.5 eq.) was added in one portion. The solution was stirred for 1 h at rt and then the solvent was removed *in vacuo*. FC (*n*-pentane/MTBE, 5:1) afforded the title compound (0.084 g, 0.31 mmol, 85%) as a red solid. Single crystals suitable for X-Ray analysis were obtained by slow evaporation of an EtOAc solution at rt. **R_F**: 0.56; **M.p.**: 110 °C; **IR** (neat): 3245m, 3063w, 2928w, 2122w, 1688s, 1592m, 1486s, 1458m, 1393w, 1360m, 1301m, 1260s, 1215s, 1173m, 1157w, 1124w, 1088w, 1070w, 1027w, 1002w, 960w, 907w, 831w, 746s, 730s, 704s, 684s, 660m, 617m, 603s, 533m, 505s; **HRMS** (ESI): $m/z = 298.0825$ calcd. for $[M+Na]^+$, found: 298.0826.

2,4-Diphenyl-6-((trimethylsilyl)buta-1,3-diyn-1-yl)-3-oxo verdazyl radical (5)



According to **GP2** with tetrazinan-3-one **S1** (200 mg, 0.53 mmol, 1.0 eq.) and 1,4-benzoquinone (98 mg, 0.91 mmol, 1.7 eq.) in CH_2Cl_2 (8 mL) for 4 h at 60 °C. FC (*n*-pentane/MTBE 20:1) afforded the title compound (113 mg, 0.31 mmol, 58%) as a dark red solid. Single crystals suitable for X-Ray analysis were obtained by slow evaporation of a solution of the sample in acetone at rt. **R_F**: 0.49; **M.p.**: 138 °C (decomp.); **IR** (neat): 2961w, 1706m, 1593w, 1486w, 1457w, 1248m, 1113m, 1026w, 893w, 843s, 767m, 744s, 711m, 689s, 647m, 604m; **HRMS** (ESI): $m/z = 394.1220, 765.2548$ calcd. for $[M+Na]^+$, $[2M+Na]^+$, found: 394.1213, 765.2560.

2,4-Diphenyl-6-((trimethylsilyl)buta-1,3-diyn-1-yl)-3-oxo verdazyl radical (6)



Verdazyl radical **5** (69 mg, 0.19 mmol, 1.0 eq.) was dissolved in acetone (3 mL) and KF (32 mg, 0.52 mmol, 3.0 eq.) was added. After 2.5 h full conversion by TLC was observed. Water (10 mL) was added and the mixture was extracted with CH₂Cl₂ (2 × 10 mL). The combined organic layers were washed with brine, dried over MgSO₄ and dried *in vacuo*. The residue was purified by MPLC using a *Reveleris*® Amino 4 g column (cyclohexane/EtOAc 1:0 to 3:1; flow rate: 14 mL/min), which afforded the title compound (34 mg, 0.11 mmol, 61%) as a brown solid. Single crystals suitable for X-Ray analysis were achieved by slow evaporation of a filtered solution of the compound in EtOAc over several days without the presence of light. **R_F**: 0.52 (*n*-pentane/MTBE 5:1); **M.p.**: > 230 °C; **IR** (neat): 3223*m*, 2228*w*, 1691*s*, 1593*w*, 1486*m*, 1458*w*, 1404*w*, 1361*w*, 1258*w*, 1236*m*, 1124*w*, 1107*w*, 1071*w*, 1029*w*, 1002*w*, 765*w*, 736*m*, 706*m*, 693*m*, 682*s*, 647*m*, 602*m*; **HRMS** (ESI): *m/z* = 322.0825 calcd. for [M+Na]⁺, found: 322.0820.

3 X-Ray Crystal Structure Analysis

X-Ray diffraction: Data sets for the compounds **3** and **4** were collected with a Nonius Kappa CCD diffractometer. Programs used: data collection, COLLECT⁶; data reduction Denzo-SMN⁷; absorption correction, Denzo⁸; structure solution SHELXS-97⁹; structure refinement SHELXL-97⁹ and graphics, XP¹⁰. For the compounds **5** and **6** the data sets were collected with a D8 Venture Dual Source 100 CMOS diffractometer. Programs used: data collection: APEX2 V2014.5-0¹¹; cell refinement: SAINT V8.34A¹¹; data reduction: SAINT V8.34A¹¹; absorption correction, SADABS V2014/2¹¹; structure solution SHELXT-2014¹²; structure refinement SHELXL-2014¹² and graphics, XP¹⁰. *R*-values are given for observed reflections, and *wR*² values are given for all reflections.

Exceptions and special features: For compound **3** one phenyl group is disordered over two positions. Several restraints (SADI, SAME, ISOR and SIMU) were used in order to improve refinement stability. The hydrogen positions at C6 atom were refined freely. No additional symmetry was found using the option "ADDSYM" from the PLATON¹³ software. CCDC-1817427 (**3**), -1817428 (**4**), -1817429 (**5**) and -1817430 (**6**) contain the supplementary crystallographic data for this paper. These data can be obtained free of charge from The Cambridge Crystallographic Data Centre via www.ccdc.cam.ac.uk/data_request/cif.

X-ray Crystal Structure Analysis of 3: formula C₁₉H₁₉N₄OSi, *M* = 347.47, red crystal, 0.20 x 0.08 x 0.03 mm, *a* = 9.6565(5), *b* = 17.9910(9), *c* = 5.8635(3) Å, β = 113.819(2) °, *V* = 931.9(1) Å³, ρ_{calc} = 1.24 gcm⁻³, μ = 0.1 mm⁻¹, empirical absorption correction (0.972 ≤ *T* ≤ 0.995), *Z* = 2, monoclinic, space group *Cm* (No. 8), λ = 0.71073 Å, *T* = 223(2) K, ω and φ scans, 4397 reflections collected (±*h*, ±*k*, ±*l*), 2193 independent (*R*_{int} = 0.053) and 1820 observed reflections [*I* > 2σ(*I*)], 185 refined parameters, *R* = 0.066, *wR*² = 0.157, max. (min.) residual electron density 0.24 (-0.17) e.Å⁻³, hydrogen atoms were calculated and refined as riding atoms. The structure was refined as an inversion twin (TWIN, BASF). The Flack parameter was refined to 0.4(3).

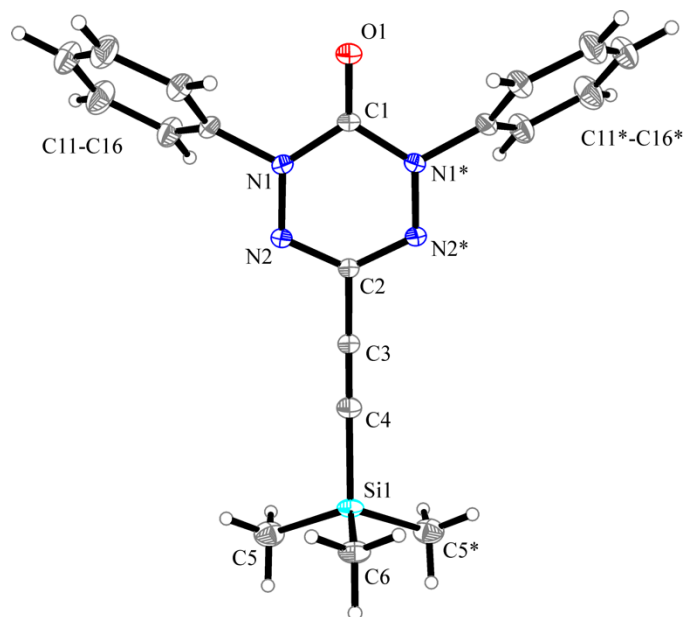


Figure S1. Molecular entity in the crystal structure of verdazyl radical **3**. Displacement ellipsoids are shown with 30% probability.

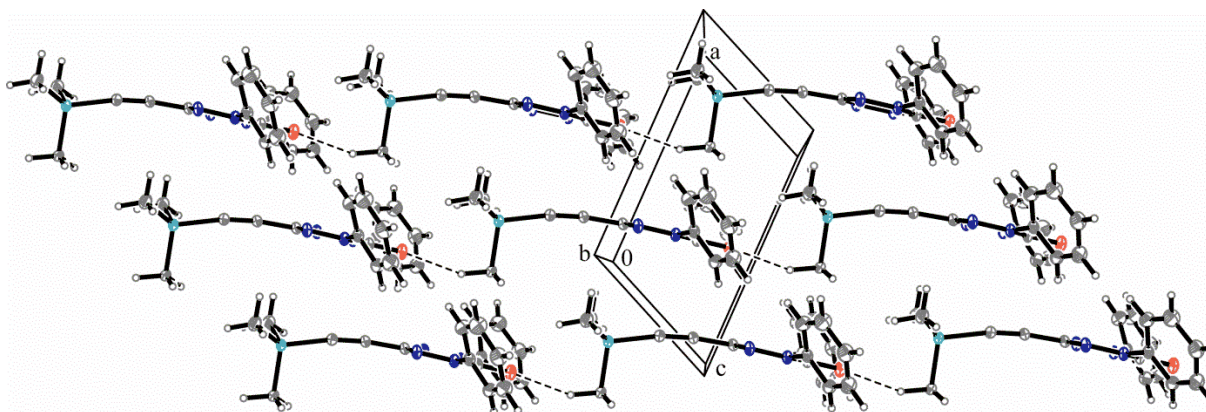


Figure S2. Crystal structure of verdazyl radical **3**. View on top of the *b*-axis.

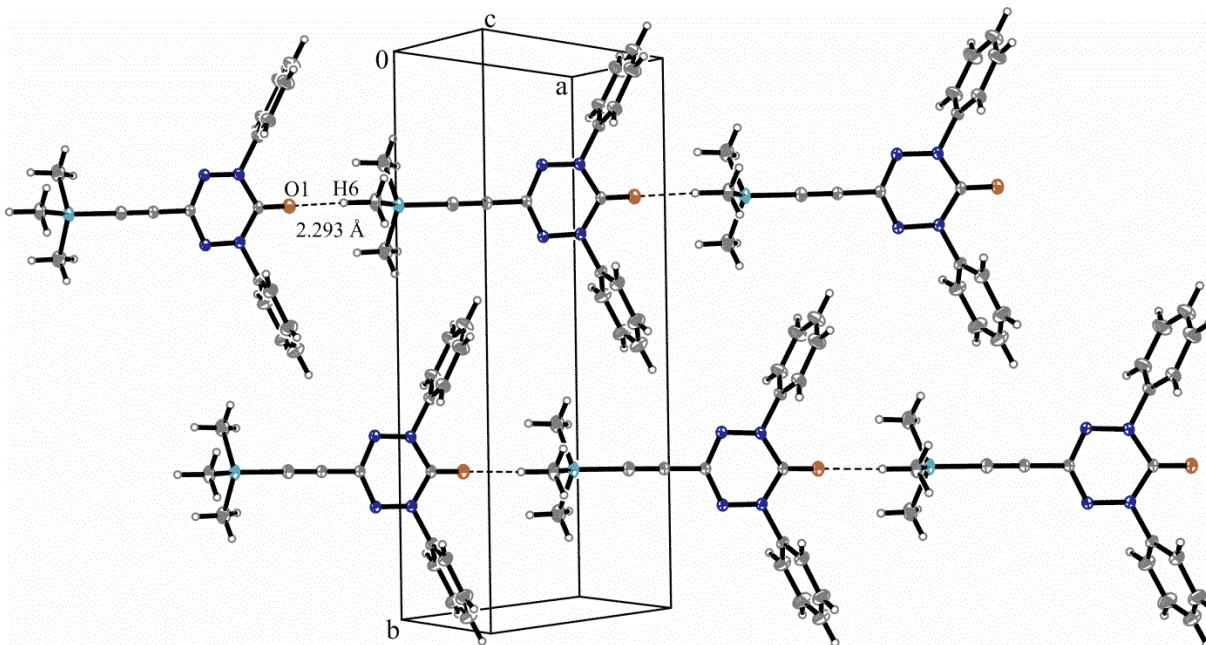


Figure S3. Crystal structure of verdazyl radical **3**. View along the *ac*-diagonal: parallel arrangement of linear chains, generated by C-H...O interactions.

X-ray Crystal Structure Analysis of 4: formula $C_{16}H_{11}N_4O$, $M = 275.29$, red crystal, $0.23 \times 0.04 \times 0.04$ mm, $a = 17.0182(6)$, $b = 20.5047(7)$, $c = 3.8678(1)$ Å, $V = 1349.7(1)$ Å³, $\rho_{\text{calc}} = 1.36$ gcm⁻³, $\mu = 0.7$ mm⁻¹, empirical absorption correction ($0.851 \leq T \leq 0.971$), $Z = 4$, orthorhombic, space group $Pna2_1$ (No. 33), $\lambda = 1.54178$ Å, $T = 223(2)$ K, ω and φ scans, 6209 reflections collected ($\pm h, \pm k, \pm l$), 2243 independent ($R_{\text{int}} = 0.045$) and 1979 observed reflections [$I > 2\sigma(I)$], 190 refined parameters, $R = 0.040$, $wR^2 = 0.098$, max. (min.) residual electron density 0.13 (-0.17) e.Å⁻³, hydrogen atoms were calculated and refined as riding atoms. The Flack parameter was refined to 0.4(4).

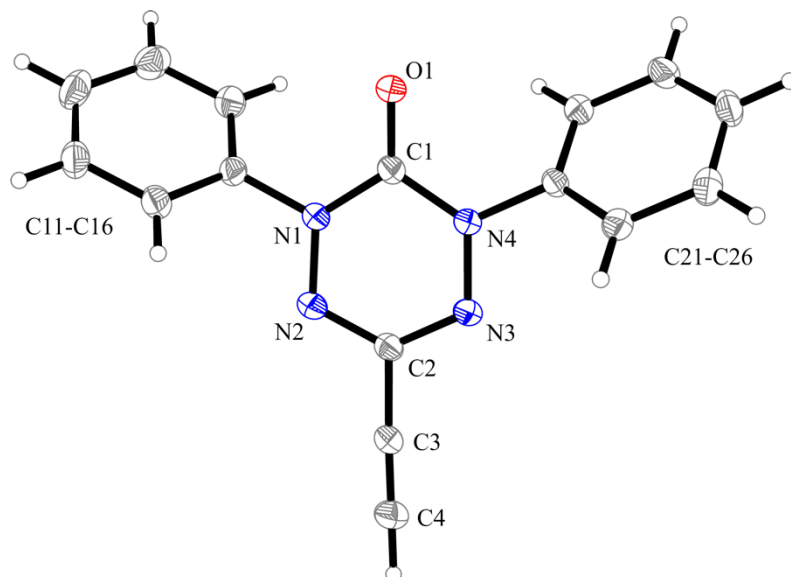


Figure S4. Molecular entity in the crystal structure of verdazyl radical **4**. Displacement ellipsoids are shown with 30% probability.

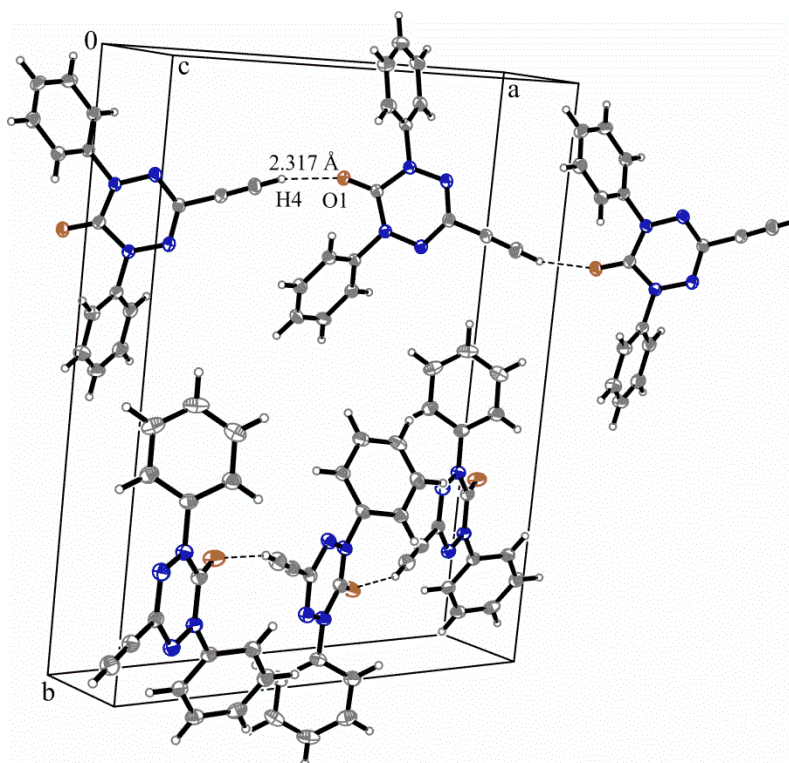


Figure S5. Crystal structure of verdazyl radical **4**. View along the *ac*-diagonal: linear chains generated by C-H...O interactions (C4-H4...O1 = 2.317 Å; 158.2°) with an angle of 54°.

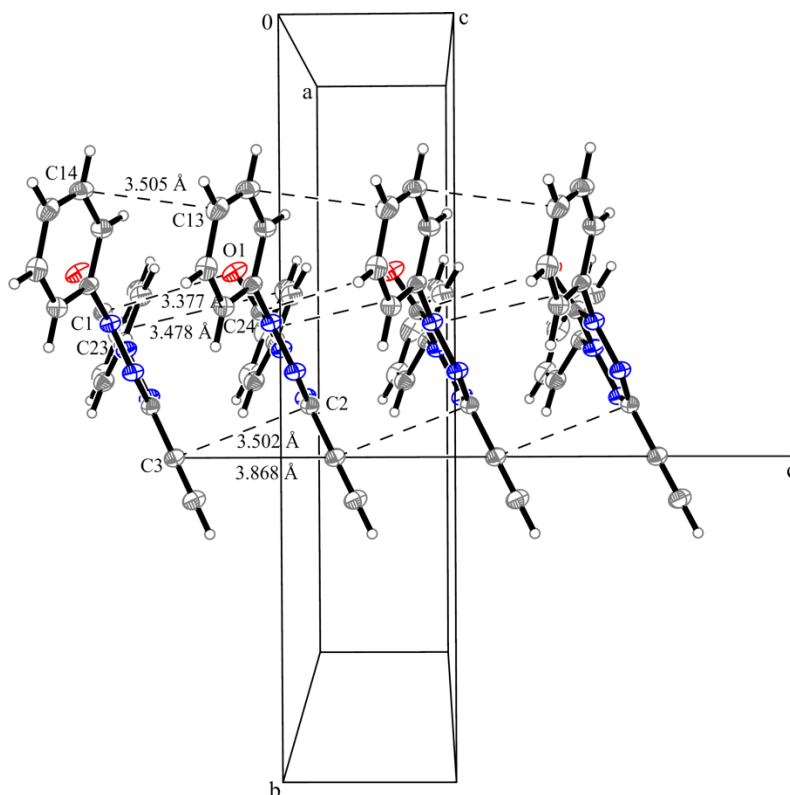


Figure S6. Excerpt of the packing diagram of verdazyl radical **4**. View in the direction of the *a*-axis.

X-ray Crystal Structure Analysis of **5 and Discussion of Magnetic Topology:** A red prism-like specimen of $C_{21}H_{19}N_4OSi$, approximate dimensions 0.097 mm x 0.212 mm x 0.216 mm, was used for the X-ray crystallographic analysis. The X-ray intensity data were measured. A total of 422 frames were collected. The total exposure time was 2.34 hours. The frames were integrated with the Bruker SAINT software package using a narrow-frame algorithm. The integration of the data using a monoclinic unit cell yielded a total of 17213 reflections to a maximum θ angle of 27.53° (0.77 \AA resolution), of which 2377 were independent (average redundancy 7.241, completeness = 99.9%, $R_{\text{int}} = 4.68\%$, $R_{\text{sig}} = 2.56\%$) and 2046 (86.07%) were greater than $2\sigma(F^2)$. The final cell constants of $a = 5.9346(2)$, $b = 16.9487(6)$, $c = 10.0933(4) \text{ \AA}$, $\beta = 99.999(2)^\circ$, $V = 999.80(6) \text{ \AA}^3$, are based upon the refinement of the XYZ-centroids of 7192 reflections above $20 \sigma(I)$ with $4.750^\circ < 2\theta < 54.93^\circ$. Data were corrected for absorption effects using the multi-scan method (SADABS). The ratio of minimum to maximum apparent transmission was 0.949. The calculated minimum and maximum transmission coefficients (based on crystal size) are 0.971 and 0.987. The structure was solved and refined using the Bruker SHELXTL

Software Package, using the space group $P2_1/m$, with $Z = 2$ for the formula unit, $C_{21}H_{19}N_4OSi$. The final anisotropic full-matrix least-squares refinement on F^2 with 144 variables converged at $R1 = 3.85\%$, for the observed data and $wR2 = 9.30\%$ for all data. The goodness-of-fit was 1.061. The largest peak in the final difference electron density synthesis was $0.31 \text{ e}/\text{\AA}^3$ and the largest hole was $-0.31 \text{ e}/\text{\AA}^3$ with an RMS deviation of $0.05 \text{ e}/\text{\AA}^3$. On the basis of the final model, the calculated density was $1.23 \text{ g}/\text{cm}^3$ and $F(000)$, 390 e^- .

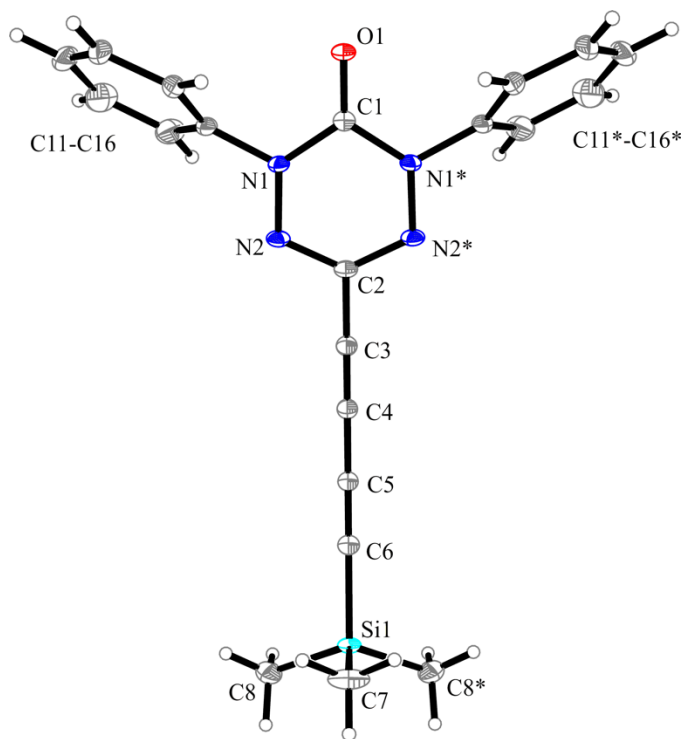


Figure S7. Molecular entity in the crystal structure of verdazyl radical **5**. Displacement ellipsoids are shown with 30% probability.

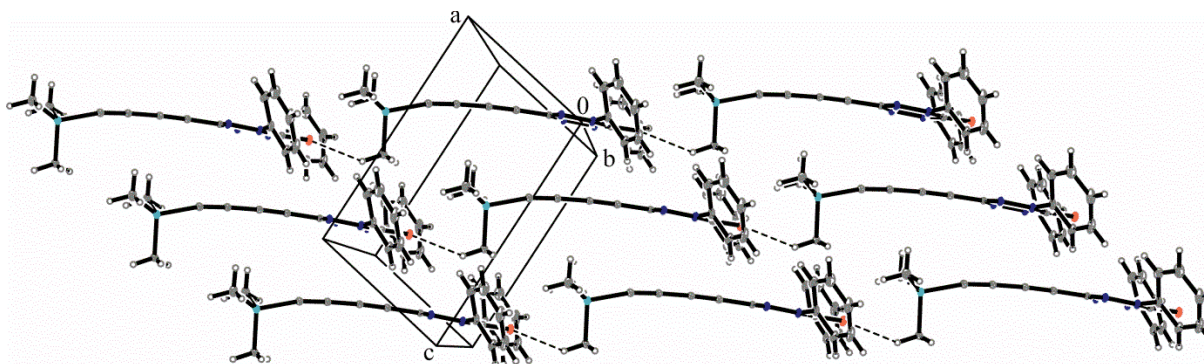


Figure S8. Crystal structure of verdazyl radical **5**. View on top of the b -axis: linear chains, generated by $\text{CH}\cdots\text{O}$ interactions ($\text{C7-H7}\cdots\text{O1} = 2.477 \text{ \AA}$; 140.1°).

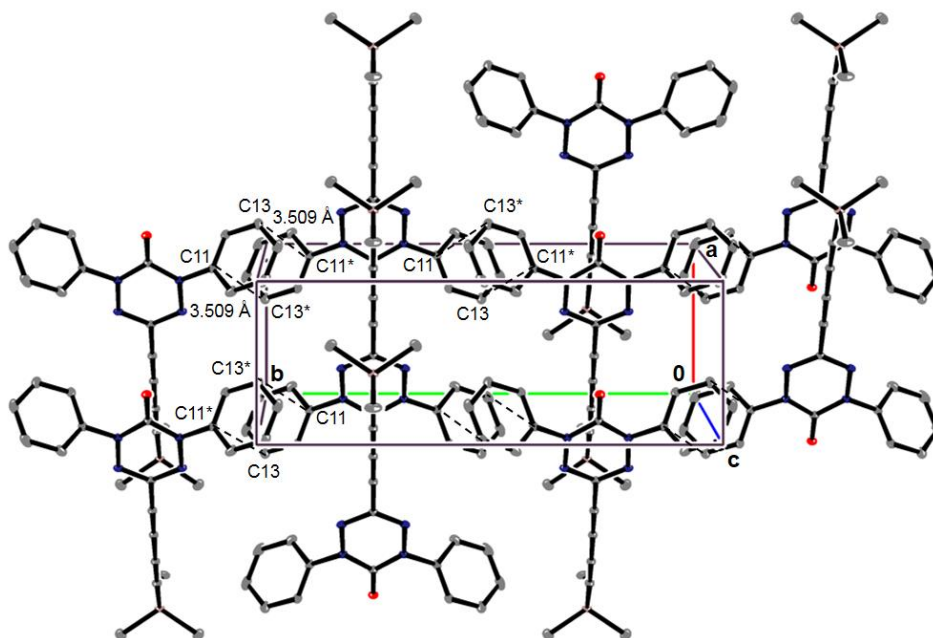


Figure S9. Crystal structure of verdazyl radical **5**. View on top of the *c*-axis: antiparallel oriented linear chains with π - π interactions between inter-chain *N*-phenyl rings (C11*...C13 and C11...C13* = 3.509 Å) representing the magnetic coupling constant J_2 , which is propagating along the *b*-axis (for a zoom-in, please see picture below). H atoms are omitted for clarity.ⁱ

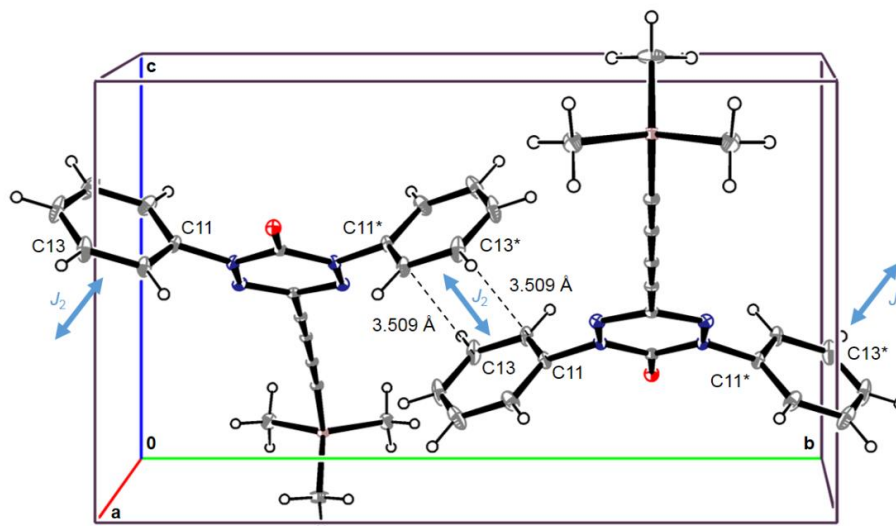


Figure S10. Excerpt of the crystal structure of verdazyl radical **5**. View on top of the *a*-axis: pair of molecules highlighting the antiferromagnetic coupling constant J_2 , propagating along the *b*-axis through π - π interactions between neighboring (inter-chain) *N*-phenyl rings.^v

ⁱ Crystal structure pictures were created with ORTEP3 for Windows; for a reference, see: Farrugia, L. J. *Appl. Crystallogr.* **2012**, *45*, 849.

X-ray Crystal Structure Analysis of 6: A red needle-like specimen of $C_{18}H_{11}N_4O$, approximate dimensions 0.040 mm x 0.081 mm x 0.152 mm, was used for the X-ray crystallographic analysis. The X-ray intensity data were measured. A total of 597 frames were collected. The total exposure time was 3.73 hours. The frames were integrated with the Bruker SAINT software package using a narrow-frame algorithm. The integration of the data using a monoclinic unit cell yielded a total of 4586 reflections to a maximum θ angle of 25.02° (0.84 \AA resolution), of which 1211 were independent (average redundancy 3.787, completeness = 99.4%, $R_{\text{int}} = 3.36\%$, $R_{\text{sig}} = 2.92\%$) and 1127 (93.06%) were greater than $2\sigma(F^2)$. The final cell constants of $a = 11.2700(8) \text{ \AA}$, $b = 16.9544(11) \text{ \AA}$, $c = 3.7589(2) \text{ \AA}$, $\beta = 96.640(2)^\circ$, $V = 713.42(8) \text{ \AA}^3$, are based upon the refinement of the XYZ-centroids of 2760 reflections above $20 \sigma(I)$ with $4.802^\circ < 2\theta < 50.14^\circ$. Data were corrected for absorption effects using the multi-scan method (SADABS). The ratio of minimum to maximum apparent transmission was 0.922. The calculated minimum and maximum transmission coefficients (based on crystal size) are 0.986 and 0.996. The structure was solved and refined using the Bruker SHELXTL Software Package, using the space group Cm , with $Z = 2$ for the formula unit, $C_{18}H_{11}N_4O$. The final anisotropic full-matrix least-squares refinement on F^2 with 119 variables converged at $R1 = 2.67\%$, for the observed data and $wR2 = 5.91\%$ for all data. The goodness-of-fit was 1.119. The largest peak in the final difference electron density synthesis was $0.12 \text{ e}^-/\text{\AA}^3$ and the largest hole was $-0.14 \text{ e}^-/\text{\AA}^3$ with an RMS deviation of $0.03 \text{ e}^-/\text{\AA}^3$. On the basis of the final model, the calculated density was 1.39 g/cm^3 and $F(000)$, 310 e⁻. The Flack parameter is meaningless and was defined to $-1.6(9)$.

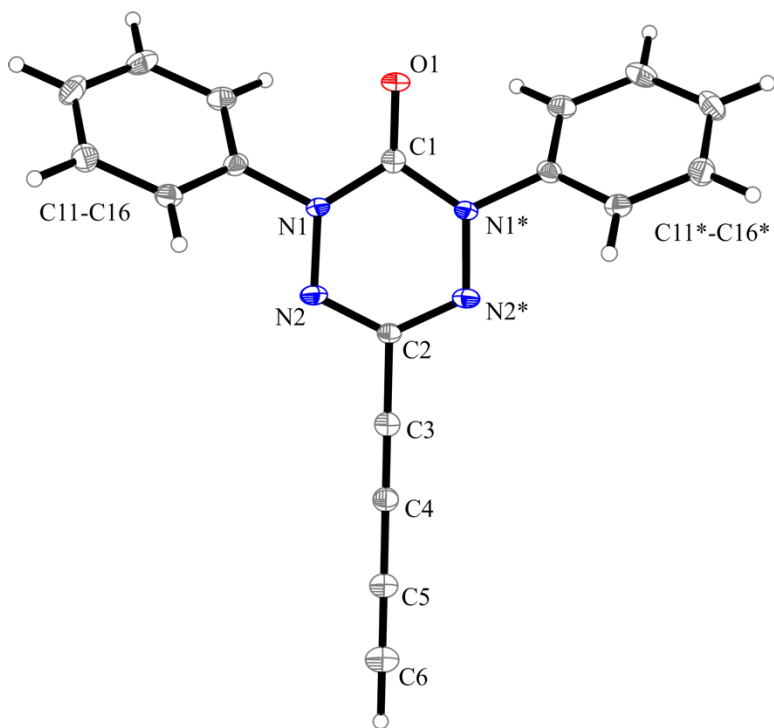


Figure S11. Molecular entity in the crystal structure of verdazyl radical **6**. Displacement ellipsoids are shown with 50% probability.

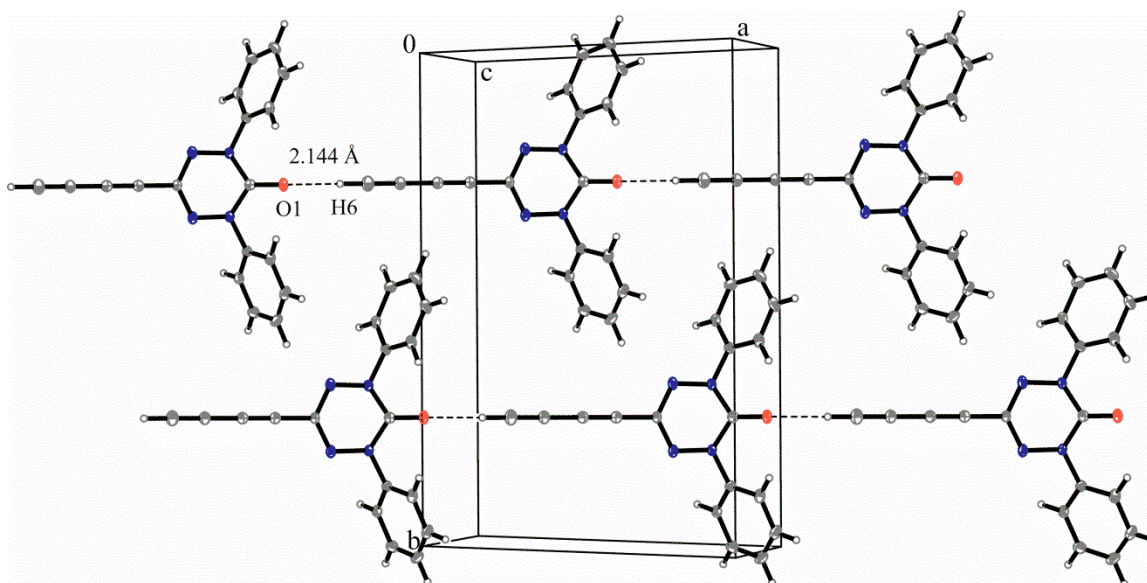


Figure S12. Crystal structure of verdazyl radical **6**. View along the *ac*-diagonal: parallel oriented linear chains generated by C-H...O interactions (C6-H6...O1, 2.144 Å; 170.8°).

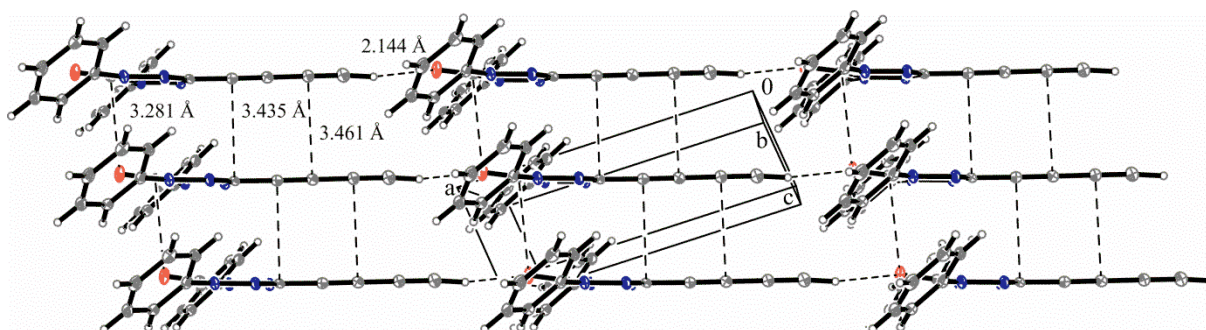


Figure S13. Crystal structure of verdazyl radical **6**. View on top of the *b*-axis.

Table S1. Summary of crystallographic data for verdazyl radicals **3–6**.

	3	4	5	6
<i>T</i> / K	223(2)	223(2)	100(2)	104(2)
empirical formula	C ₁₉ H ₁₉ N ₄ OSi ^{•+}	C ₁₆ H ₁₁ N ₄ O ^{•+}	C ₂₁ H ₁₉ N ₄ OSi	C ₁₈ H ₁₁ N ₄ O ^{•+}
formula weight [g/mol]	347.47	275.28	371.49	299.31
crystal size [mm ³]	0.20 × 0.08 × 0.03	0.23 × 0.04 × 0.04	0.097 × 0.212 × 0.216	0.040 × 0.081 × 0.152
color, habit	red	red	red prism	red needle
crystal system	monoclinic	orthorhombic	monoclinic	monoclinic
space group	<i>Cm</i> (No. 8)	<i>Pna</i> 2 ₁ (No. 33)	<i>P</i> 2 ₁ / <i>m</i> (No. 11)	<i>Cm</i> (No. 8)
<i>a</i> [Å]	9.6565(5)	17.0182(6)	5.9346(2)	11.2700(8)
<i>b</i> [Å]	17.9910(9)	20.5047(7)	16.9487(6)	16.9544(11)
<i>c</i> [Å]	5.8635(3)	3.8678(1)	10.0933(4)	3.7589(2)
β	113.819(2) ^o	90	99.999(2)	96.640(2)
volume [Å ³]	931.90(8)	1349.68	999.80(6)	713.418

4 EPR Spectroscopy

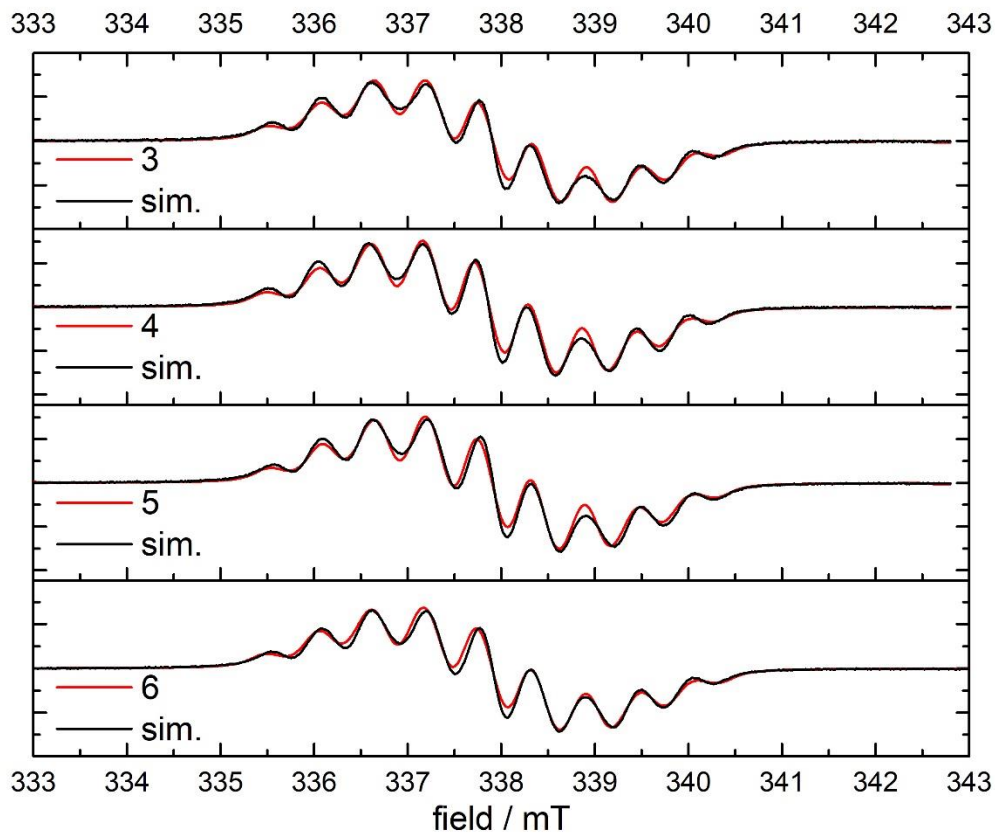


Figure S14. EPR spectrum of 0.5 mM solutions in toluene of the studied verdazyl radicals (black) and simulations (red)

Table S2. Summary of the EPR measurements of **3–6** in 0.1 mM degassed toluene. A_{iso} values (in MHz) and g -values are listed. Hyperfine couplings to the protons are not considered, because previous work indicated that their effect only contributes an overall line broadening of the simulated curves.

	$A(N-2,4)$	$A(N-1,5)$	g -value
3 ¹⁴	17.53	13.51	2.0037
4	17.13	13.52	2.0037
5	17.31	13.46	2.0038
6	17.67	13.55	2.0037

5 Physical Properties

Experimental

Magnetic Properties: The radical compounds **3–6** were packed in PE capsules in air and attached to the sample holder rod of a Vibrating Sample Magnetometer unit (VSM) for measuring the magnetization $M(T)$ in a Quantum Design Physical-Property-Measurement-System (PPMS). The samples were investigated in the temperature range of 2.5-300 K with magnetic flux densities up to 80 kOe. The magnetization isotherms shown in Figure S16 were recorded at 5 and 2 K on a Quantum Design Magnetic Property Measurement System (MPMS) in DC scan mode. For both temperatures the following flux density profile was used. First the magnetic flux density was increased stepwise ($\Delta H = 5$ kOe) from 0 kOe to 50 kOe. Then, starting with 47.5 kOe the magnetic flux density was decreased stepwise ($\Delta H = 5$ kOe) to 2.5 kOe.

Results and Discussion

Magnetic Properties: For the radical compounds **3–6** zero-field-cooled measurements at external fields of 10 kOe were conducted. The magnetic susceptibility χ and its inverse χ^{-1} from compounds **3, 5, 6** are depicted in Figures S15, S17 (top panel). From the inverse susceptibility the Curie constant C , the paramagnetic Weiss temperature θ_P and the diamagnetic contribution were derived using the modified Curie-Weiss law. The extracted parameters are listed in Table S3. From the low field measurements (100 Oe), conducted in zero-field-cooled / field-cooled mode, the Néel temperatures of compound **3** (Figure 3, bottom panel) and **5** (Figures S17, middle panel) were derived. No bifurcation was observed, in line with antiferromagnetism. χT plots were used to interpret the dominant interactions. Compound **5** exhibits antiferromagnetic interactions (Figure S17, bottom panel), in line with the observed antiferromagnetic ordering. Compound **6** in contrast exhibits ferromagnetic interactions (Figure S18), as observed from the χT plots. Finally magnetization isotherms of compound **4** were recorded at 2 and 5 K (Figure S16). In line with the χT plot (Figure 4), the magnetization rises quite rapidly at 2 K, while the 5 K isotherm exhibits only a slight curvature, as observed for paramagnetic materials.

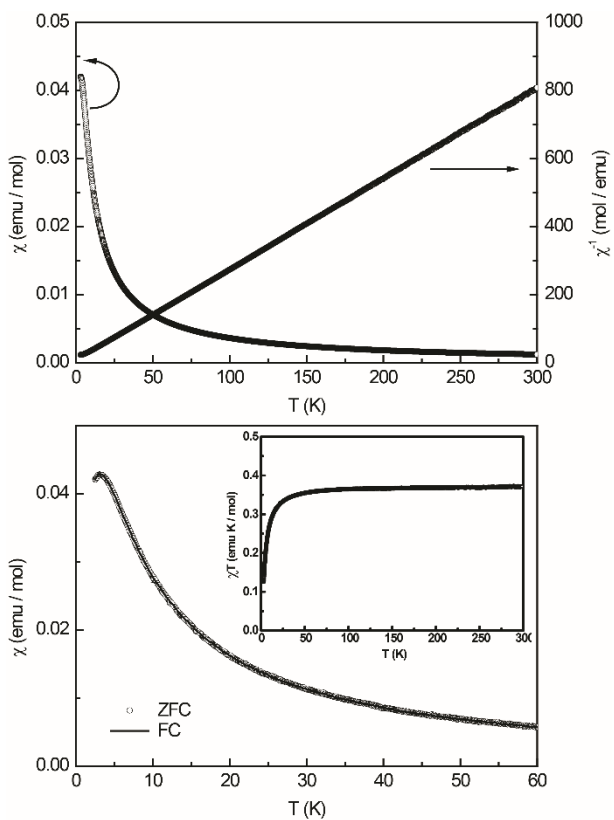


Figure S15. Magnetic properties of compound **3**. Top: temperature dependence of the magnetic susceptibility data χ and its inverse χ^{-1} measured at 10 kOe; bottom: temperature dependence of the magnetic susceptibility measured in zero-field-cooled / field-cooled mode at 100 Oe; inset: χT versus T plot, indicating antiferromagnetic interactions.

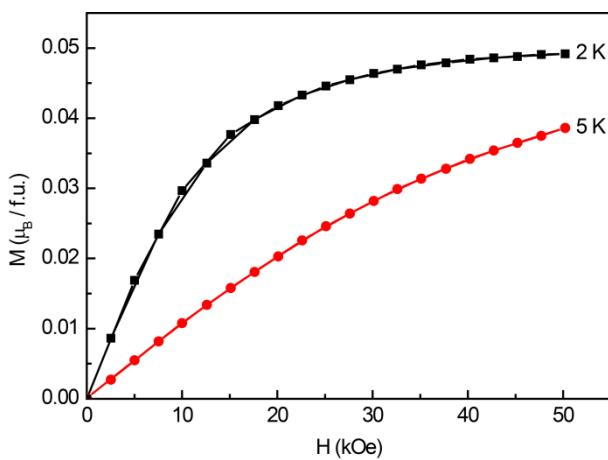


Figure S16. Magnetization isotherms $M(H)$ of verdazyl radical **4**, recorded at 2 and 5 K.

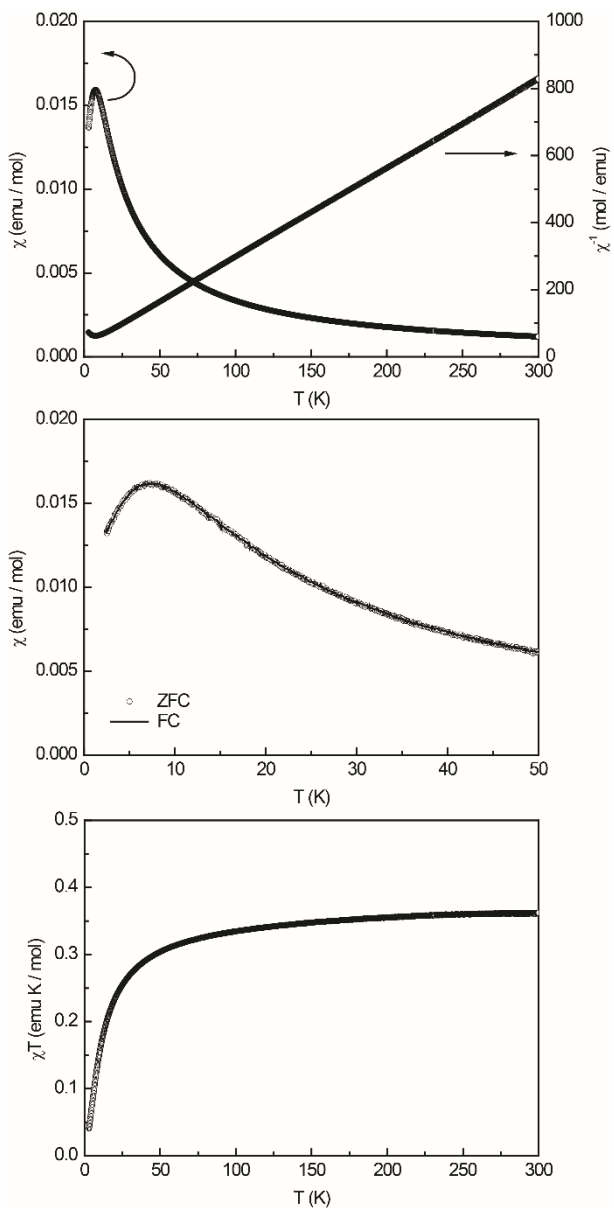


Figure S17. Magnetic properties of compound **5**. Top: temperature dependence of the magnetic susceptibility data χ and its inverse χ^{-1} measured at 10 kOe; middle: temperature dependence of the magnetic susceptibility measured in zero-field-cooled / field-cooled mode at 100 Oe; bottom: χT versus T plot, indicating antiferromagnetic interactions.

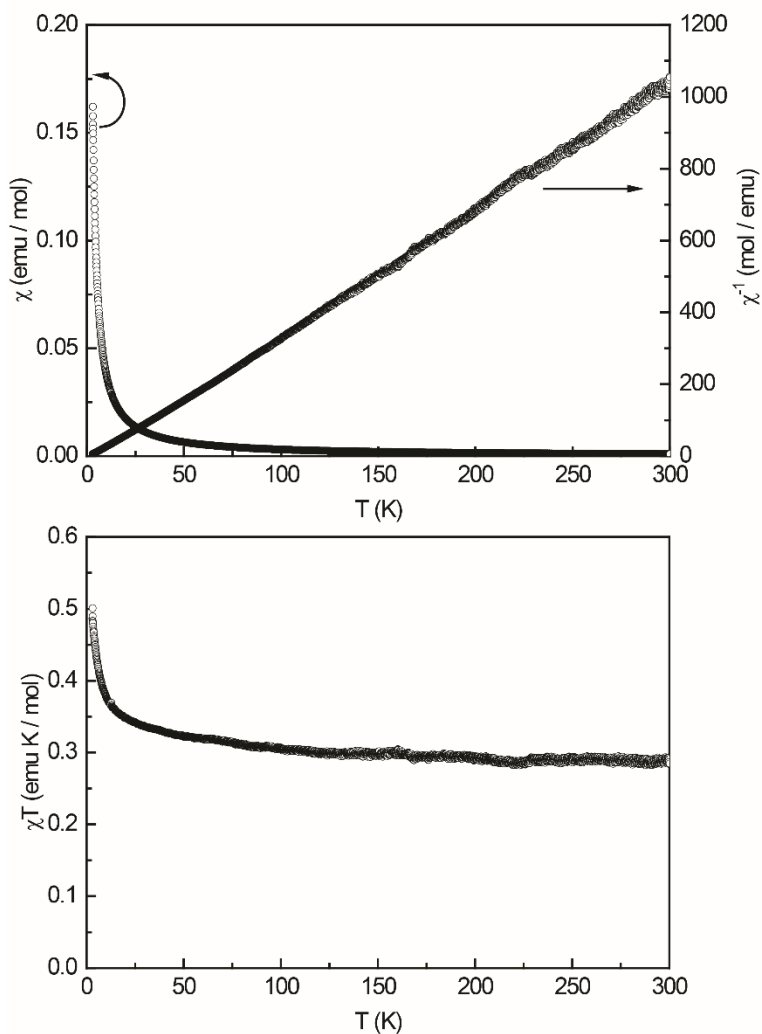


Figure S18. Magnetic properties of verdazyl radical **6**. Top: temperature dependence of the magnetic susceptibility data χ and its inverse χ^{-1} measured at 10 kOe; bottom: χT versus T plot, indicating ferromagnetic interactions.

Table S3. Summary of experimental and theoretical magnetization data.

Radical	calcd. J (cm^{-1})	χ_{dia} (emu mol^{-1})	C (K)	θ (K)	T_N (K)
3	-3.30	-311×10^{-6}	0.372	-2.4(1)	3.1(1)
4	+4.40	-493×10^{-6}	0.375	+2.8(1)	–
4 (aged sample)	+4.40		0.303	+1.9(1)	–
5	-6.01	-348×10^{-6}	0.378	-12.8(1)	7.1(1)
	-1.37				
6	+5.57	-522×10^{-6}	0.295	+4.0(1)	–

6 Theoretical Calculations

Calculation of magnetic exchange coupling constants and simulation of magnetic susceptibilities

For the simulations of magnetic susceptibilities in dependence of the temperature we made use of our implementation¹⁵ of the first-principles bottom-up approach.^{16,17} The procedure is based on the Heisenberg Hamiltonian,

$$\hat{H} = -2 \sum_{i < j} J_{ij} \hat{S}_i \hat{S}_j,$$

in which pairs of local spins \hat{S}_i on sites i interact with each other via a coupling constant J . Within the procedure first, the crystal structure is analyzed for possibly interacting pairs of molecules based on a distance criterion. Next, the magnetic exchange coupling constants are calculated with the broken symmetry density functional theory approach. For these calculations, the ORCA program system¹⁸ is used with the PBE0 functional¹⁹ and the minimally augmented Def2-TZVP basis set²⁰. Based on the results, magnetic models are generated, for which the Heisenberg Hamiltonian matrix is set up and diagonalized. The resulting spin states are then used to simulate the magnetic susceptibility according to the Boltzmann distribution. Finally, the simulations need to be tested for convergence with respect to the model size.

All radicals presented in the main article can be described by a linear chain model with a single coupling constant. In the corresponding simulations, a chain length of 12 molecules can be simulated without significant computational effort. A comparison to shorter chains (11 or 10 molecules) clearly shows that the results are sufficiently converged with respect to the chain length. For the simulation of the antiferromagnetically coupled radicals **3** and **5**, an even number of molecules must be used in all models in order to enable the possibility to form a singlet state, which is the ground state in those systems.

In the main article, results for antiferromagnetically interacting systems have been plotted as molar susceptibility versus temperature while those for ferromagnetically interacting systems have been plotted as molar susceptibility times temperature versus temperature, as is usual in the community. The respectively other representations are shown in Figures S19-S22.

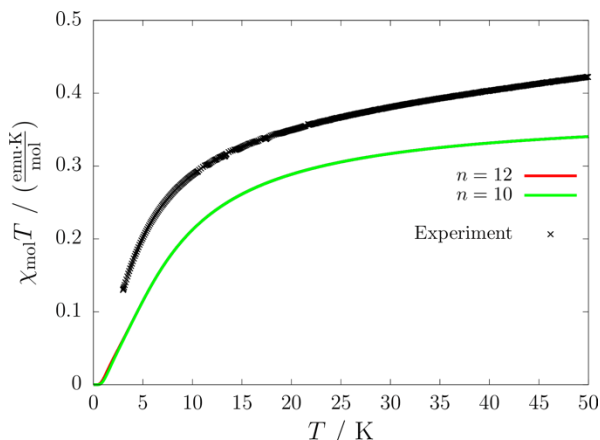


Figure S19: Computationally predicted magnetic susceptibility, in terms of χT , of **3** for magnetic models with periodically repeating chains of length $n=12$ and $n=10$ molecules in comparison with the experimental data.

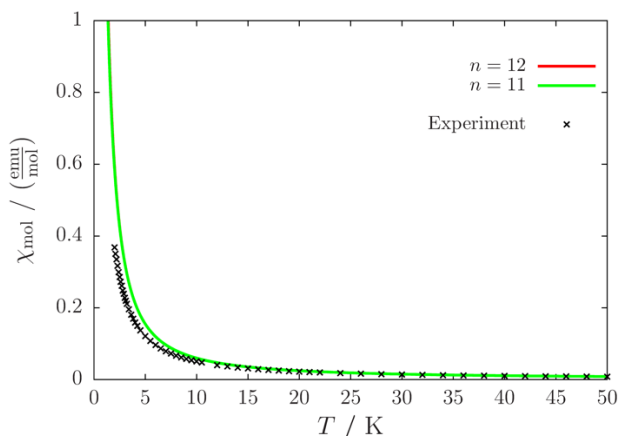


Figure S20: Computationally predicted magnetic susceptibility of **4** for magnetic models with periodically repeating chains of length $n=12$ and $n=11$ molecules in comparison with the experimental data.

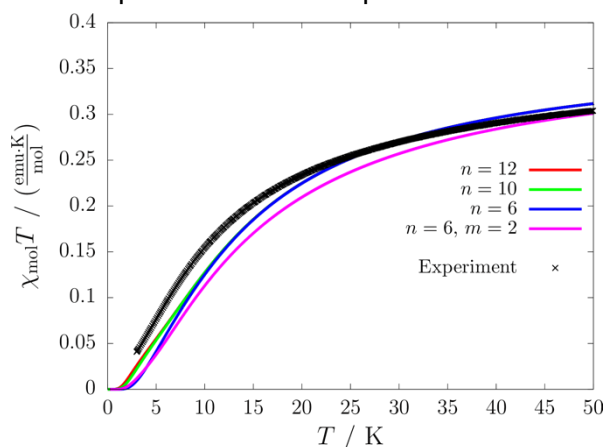


Figure S21: Comparison of the computationally predicted magnetic susceptibility, in terms of χT , of **5** for periodically repeating linear chains of different lengths n and a periodic net model with $n=6$ molecules into the a -axis and $m=2$ molecules into the b -axis with the experimental data.

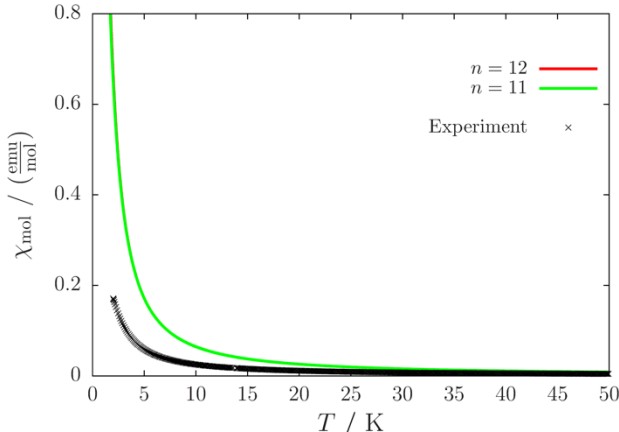


Figure S22: Comparison of the computationally predicted magnetic susceptibility of **6** for periodic linear chain models with $n=12$ and $n=11$ molecules to the experimental data.

For radical **5**, a second coupling constant with a non-negligible strength has been found. Thus, in addition to the simulation of a single chain we performed a simulation including interactions into the b -axis promoting the magnetic topology to a two-dimensional net. Although the results are clearly influenced by this additional coupling, no qualitative change can be observed in the simulations when advancing from a chain model to a net model. Thus, in this case the model of a linear chain can be considered a reasonable approximation. Due to the dramatically rising computational effort for simulations with an increasing number of magnetic sites in the model, we were not able to simulate converged results into both directions of periodic interactions for the

two-dimensional net model. However, the error due to an incomplete convergence can be estimated to be smaller than the deviation from the experimental data by comparison of the results for magnetic models of different sizes (see Figure S21 and Figure 9 in the main article).

Radical **6** shows a Curie constant deviating significantly from the theoretically expected value, which can be explained by partial degradation of the compound. To take this into account, the simulations shown in Figure 10 of the main article have been modified by scaling the susceptibility by the ratio of expected and observed Curie constants. In Figure S23 the scaled and unscaled simulations are compared. Clearly, the scaling leads to a significantly better agreement with the experimental data. However, the presence of impurities does have further implications which are neglected in this correction. While with little or no impurities it is an excellent approximation to assume infinitely long Heisenberg chains (which is implicitly assumed in our simulations due to periodic boundary conditions), a large number of impurities will lead to significantly shorter interaction chains. This could be taken into account by a statistical distribution of chains with limited length. We found, however, that distributions with chain lengths of up to 14 magnetic sites are not able to describe the experiment better than the scaled, periodic simulations (results not shown). The unfavourable scaling of the size of the Heisenberg Hamiltonian with the number of magnetic sites prevents simulations of models with a sufficient size for a good reproduction of the experimental data without periodic boundary conditions.

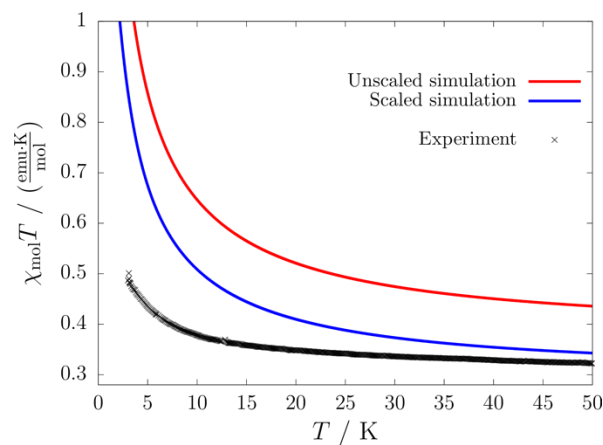


Figure S23: Comparison of the scaled and unscaled computationally predicted magnetic susceptibility of **6** for periodic linear chain models with $n=12$ molecules to the experimental data.

Calculation of the orbitals and spin populations of molecules 3–6

For compounds **3**, **4**, **5** and **6**, single point calculations have been performed to obtain representations of the singly occupied molecular orbital (SOMO) responsible for the magnetic interactions as well as the spin populations. The molecular structures as obtained from the crystal structures have been used for this purpose without further optimization. We employed the ORCA program system¹⁸ using the PBE0 functional¹⁹ and the minimally augmented Def2-TZVP basis set²⁰ to obtain the SOMOs. The results are shown in Figure 6 of the main article (radical **4**) and Figure S23.

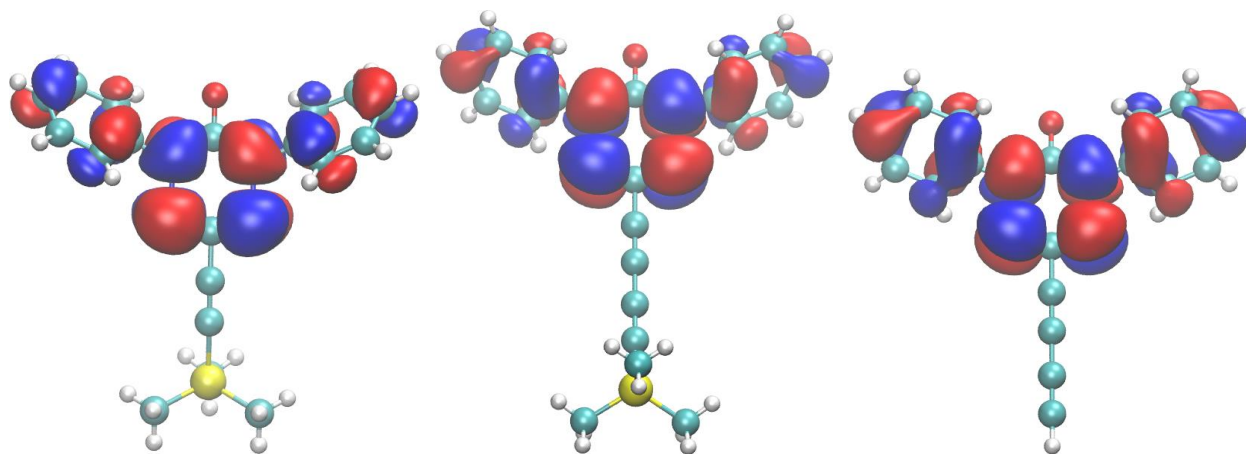


Figure S24: Singly occupied molecular orbital (SOMO) of compounds **3** (left), **5** (center) and **6** (right). Blue: positive values; red: negative values; isovalue: 0.02.

We obtained spin populations according to a Bader partitioning²¹ by performing calculations with ADF²² using the PBE0 functional¹⁹ and the TZ2P basis set.²³ The spin populations of the verdazyl heterocycle are summarized in Table S4. All other spin populations had an absolute value smaller than 0.1.

Table S4. Calculated spin densities of the molecules **3–6**.

	N1	N2	N4	N5	C3	C6
3	0.19	0.37	0.36	0.18	-0.11	-0.01
4	0.18	0.36	0.36	0.18	-0.10	-0.01
5	0.18	0.36	0.36	0.18	-0.10	-0.01
6	0.19	0.37	0.37	0.19	-0.11	-0.01

Model Calculations on a Pair of Chain Molecules in the Crystal Structure of Verdazyl Radical **4**

For the model calculations on two chain molecules of **4**, an excerpt from the crystal structure of compound **4** was taken. The vertical distance v is defined as the distance between atom O1 and the C4a-O1a molecular axis of the other molecule, which was calculated by the following equation, with δ being the C4a-O1a-O1 angle and d_{O1A-O1} being the intermolecular distance between atoms O1 and O1a (cp. Figure 5, top in the main article).

$$v = \sin(\delta) \cdot d_{O1A-O1}$$

Starting from the orientation as present in the crystal, we chose in total 11 $\Delta v = 0.05 \text{ \AA}$ steps in both positive (i.e. molecules are moved away from each other) and negative directions (i.e. molecules are moved towards each other). The horizontal shift Δh is defined as the relative shift of the C4-O1 molecular axis with respect to the arrangement in the crystal. We chose in total 19 $\Delta h = 0.3 \text{ \AA}$ steps ranging from $\Delta h = -1.8 \text{ \AA}$ (molecules are shifted towards each other) to $\Delta h = +3.6 \text{ \AA}$ (molecules are shifted away from each other). In total, we performed 209 calculations. The results are summarized in Table S5 and depicted in Figure S24.

Table S5. Matrix representing the magnetic coupling constant J (in cm^{-1}) dependence on the horizontal shifts (Δh) and vertical shifts (Δv) in two chain molecules of compound **4**. The coupling constant originating from the X-Ray structure of **4** is highlighted in bold.

$\Delta v / \text{\AA}$	$\Delta h / \text{\AA}$																		
	-1.8	-1.5	-1.2	-0.9	-0.6	-0.3	0	0.3	0.6	0.9	1.2	1.5	1.8	2.1	2.4	2.7	3	3.3	3.6
-0.25	-943.38	-769.97	-528.53	-272.91	-86.01	-0.41	11.91	-2.68	-14.84	-17.16	-12.68	-6.97	-3.56	-2.84	-3.39	-3.97	-3.82	-2.95	-1.78
-0.20	-800.64	-661.01	-455.95	-238.45	-78.13	-2.42	10.60	-0.68	-11.31	-13.90	-10.28	-5.56	-3.04	-2.49	-3.00	-3.49	-3.35	-2.60	-1.61
-0.15	-678.42	-566.31	-392.92	-208.26	-70.73	-4.05	9.09	0.45	-8.69	-11.13	-8.16	-4.53	-2.62	-2.20	-2.65	-3.05	-2.93	-2.30	-1.45
-0.10	-574.54	-484.69	-338.49	-181.78	-63.84	-5.38	7.47	0.97	-6.67	-8.71	-6.37	-3.70	-2.27	-1.96	-2.33	-2.66	-2.56	-2.04	-1.30
-0.05	-486.65	-414.73	-291.58	-158.52	-57.45	-6.44	5.88	1.17	-4.99	-6.60	-4.91	-3.05	-1.99	-1.47	-2.05	-2.32	-2.24	-1.81	-1.18
0	-412.39	-354.74	-251.07	-138.00	-51.59	-7.23	4.46	1.27	-3.51	-4.84	-3.80	-2.57	-1.75	-1.54	-1.79	-2.01	-1.96	-1.61	-1.06
0.05	-349.49	-303.20	-215.93	-119.89	-46.26	-7.73	3.33	1.43	-2.22	-3.45	-2.99	-2.22	-1.52	-1.34	-1.55	-1.74	-1.73	-1.43	-0.95
0.10	-295.94	-258.70	-185.35	-103.99	-41.43	-7.95	2.51	1.67	-1.17	-2.42	-2.41	-1.93	-1.33	-1.17	-1.34	-1.52	-1.53	-1.27	-0.85
0.15	-250.18	-220.19	-158.72	-90.13	-37.07	-7.91	1.94	1.86	-0.42	-1.70	-2.02	-1.65	-1.13	-1.00	-1.15	-1.34	-1.35	-1.11	-0.76
0.20	-211.10	-186.96	-135.69	-78.16	-33.15	-7.67	1.50	1.91	0.07	-1.24	-1.72	-1.37	-0.93	-0.85	-1.00	-1.18	-1.19	-0.97	-0.67
0.25	-177.95	-158.54	-115.96	-67.84	-29.59	-7.29	1.09	1.82	0.35	-0.95	-1.44	-1.08	-0.74	-0.74	-0.89	-1.05	-1.04	-0.85	-0.58

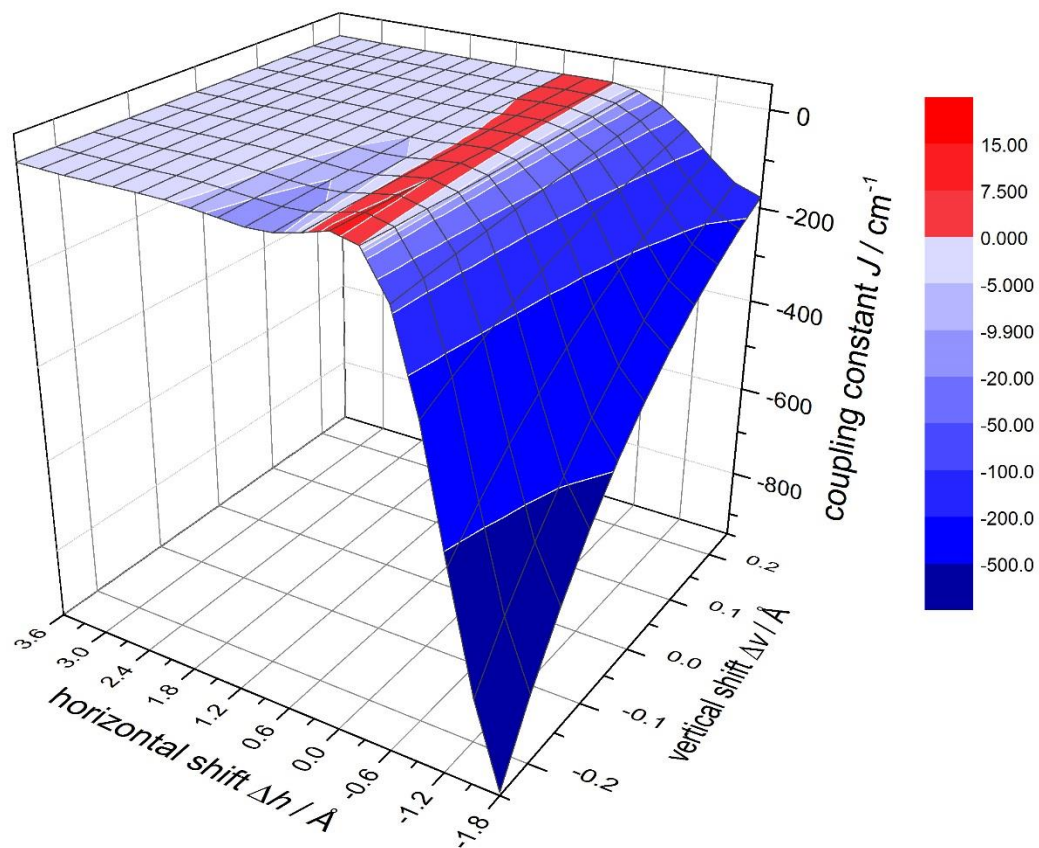


Fig. S25. Complete picture of the model calculations for two chain molecules of **4** (cp. Figure 5, bottom in the main article). Dependence of the magnetic coupling constant J (in cm^{-1} ; with $J > 0$: ferromagnetic interactions, $J < 0$: antiferromagnetic interaction) on the vertical and horizontal shifts. The origin ($\Delta v = 0$ and $\Delta h = 0$) marks the X-Ray crystallographic data of compound **4**.

7 UV/Vis Absorption Spectroscopy

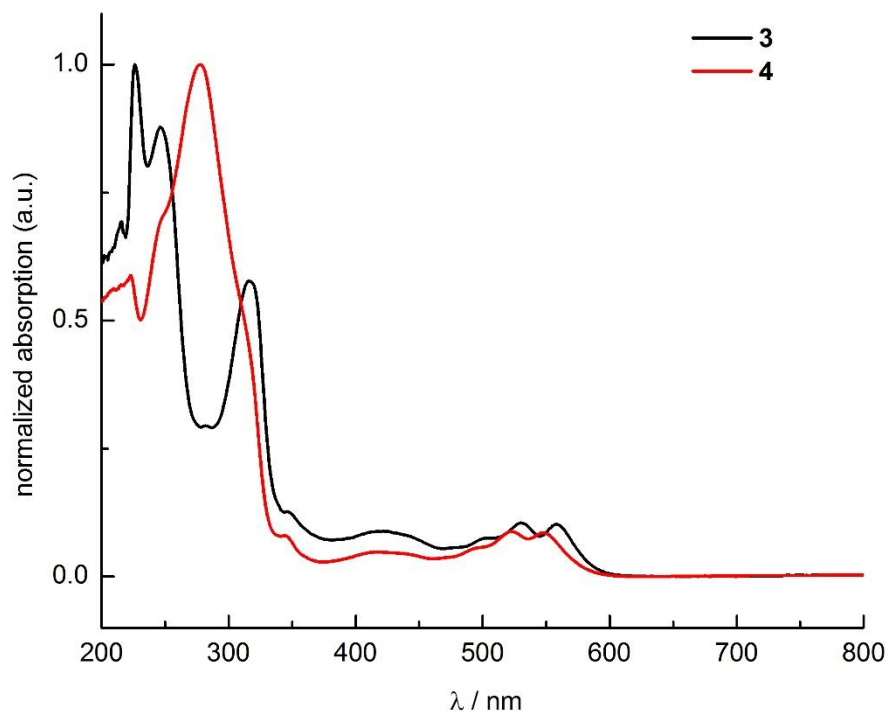


Figure S26. Absorption spectra of verdazyl radicals **3** and **4**.

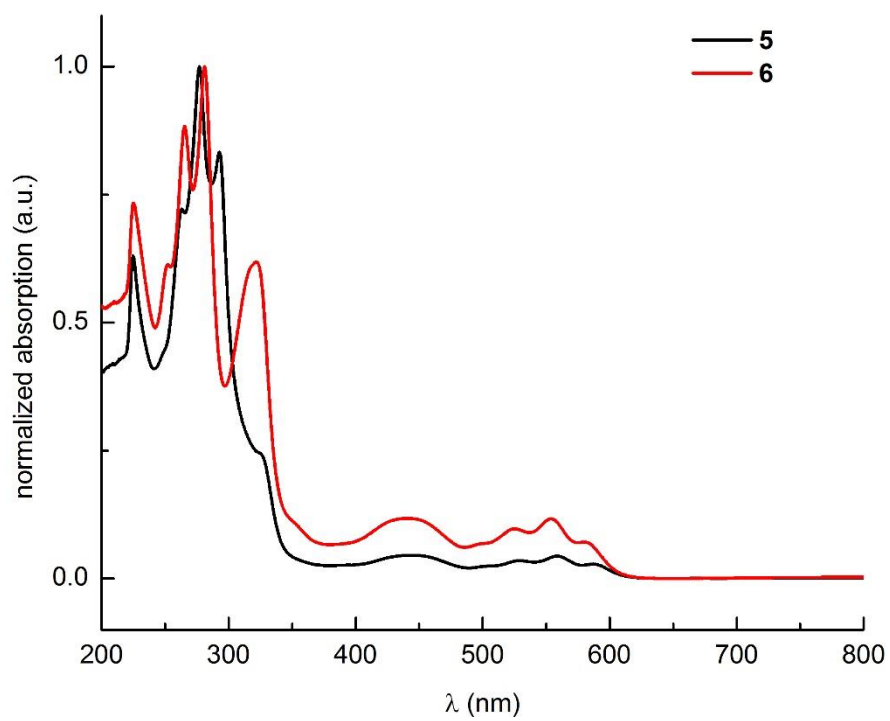


Figure S27. Absorption spectra of verdazyl radicals **5** and **6**.

Table S6. Summary of the UV/Vis absorption spectral data for verdazyl radicals **3–6**.

	$\lambda_{\max,1} / \text{nm}$	$\lambda_{\max,2} / \text{nm}$
3	421	530
4	418	523
5	443	554
6	443	558

In the visual region of the UV/Vis spectra we noticed for each verdazyl radical two absorption maxima along with vibronic shoulders. Compared to the directly substituted monoacetylene verdazyls with absorption maxima for **3** at 421 nm and 530 nm (418 nm and 523 nm for **4**) the diacetylene verdazyls **5** and **6** show slightly red shifted absorption maxima at 443 nm and around 555 nm, probably due to a higher lying HOMO π -orbital.

8 Cyclic Voltammetry Measurements

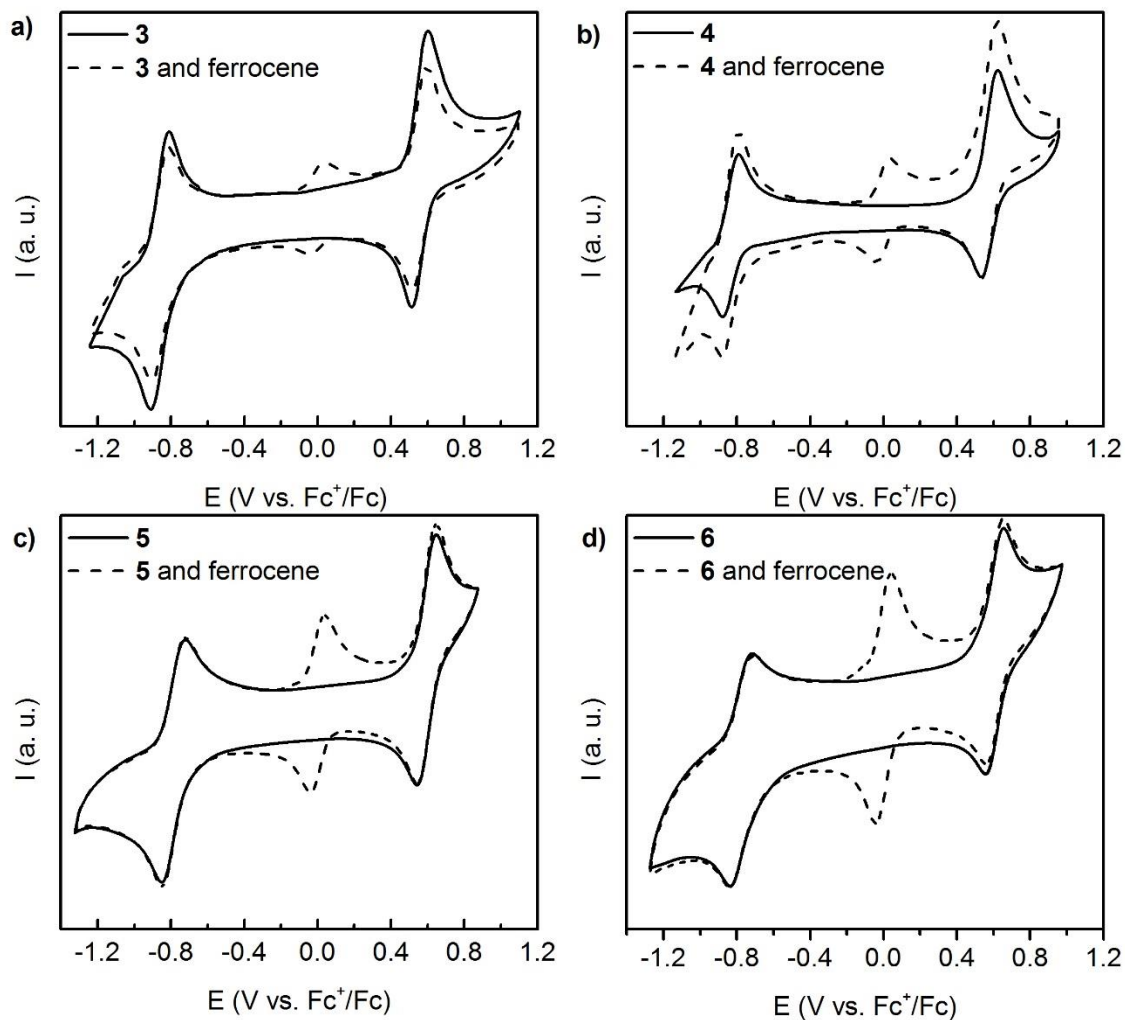


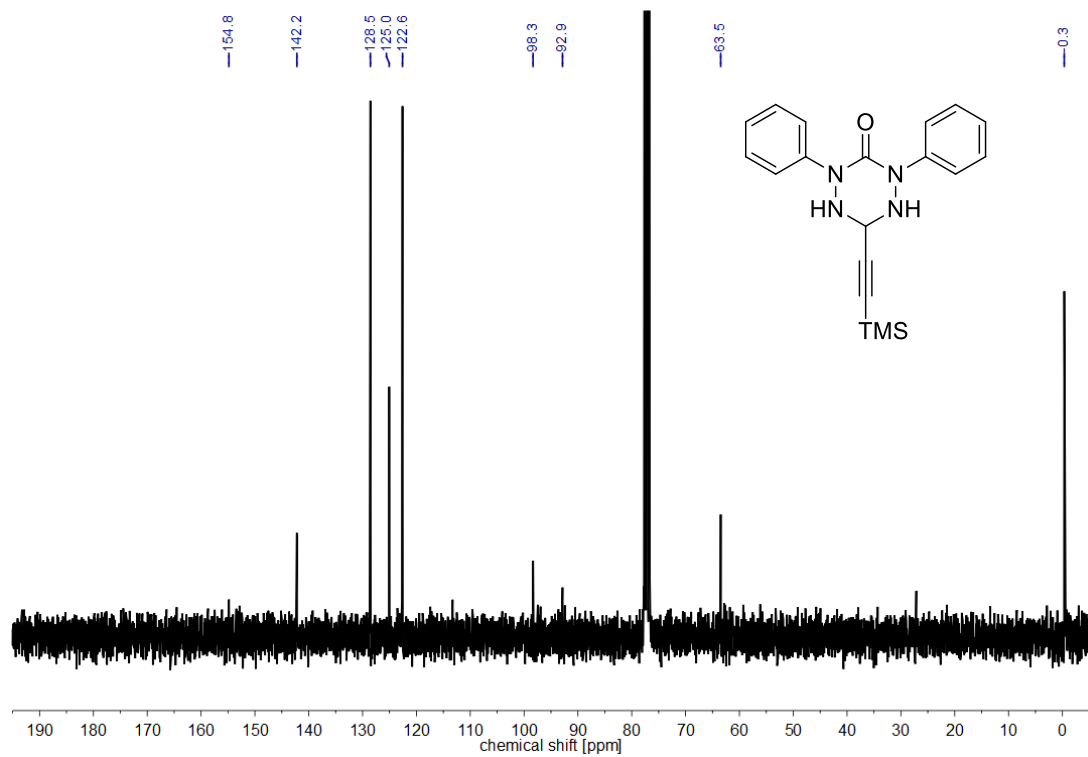
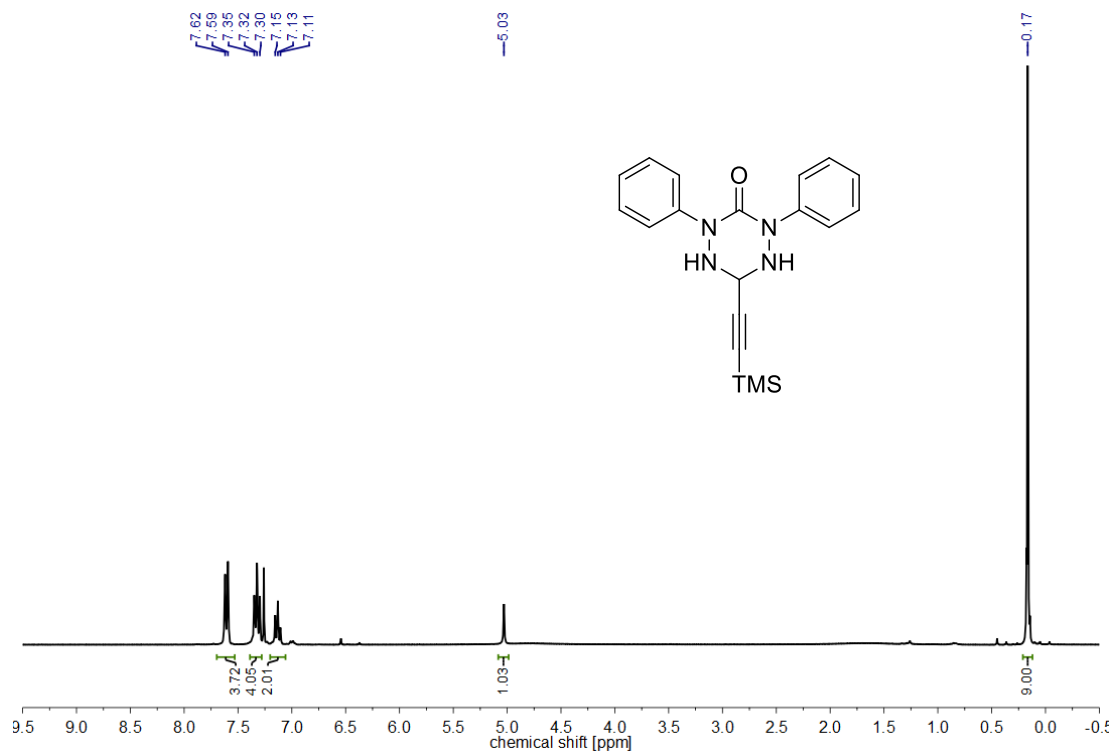
Figure S28. Cyclic voltammetry measurements for all studied verdazyl radicals: a) **3**, b) **4**, c) **5**, d) **6** measured with TBABF₄ (0.1 M in MeCN) as an electrolyte; ferrocene was used as an internal standard and its redox potential is set to 0 V; scan rate = 0.1 V s⁻¹.

Table S7. Summary of the cyclic voltammetry measurements of the verdazyl radicals **3–6** in degassed MeCN (0.1 M TBABF₄) against Fc⁺/Fc, measured at scan rates of 0.1 V s⁻¹.

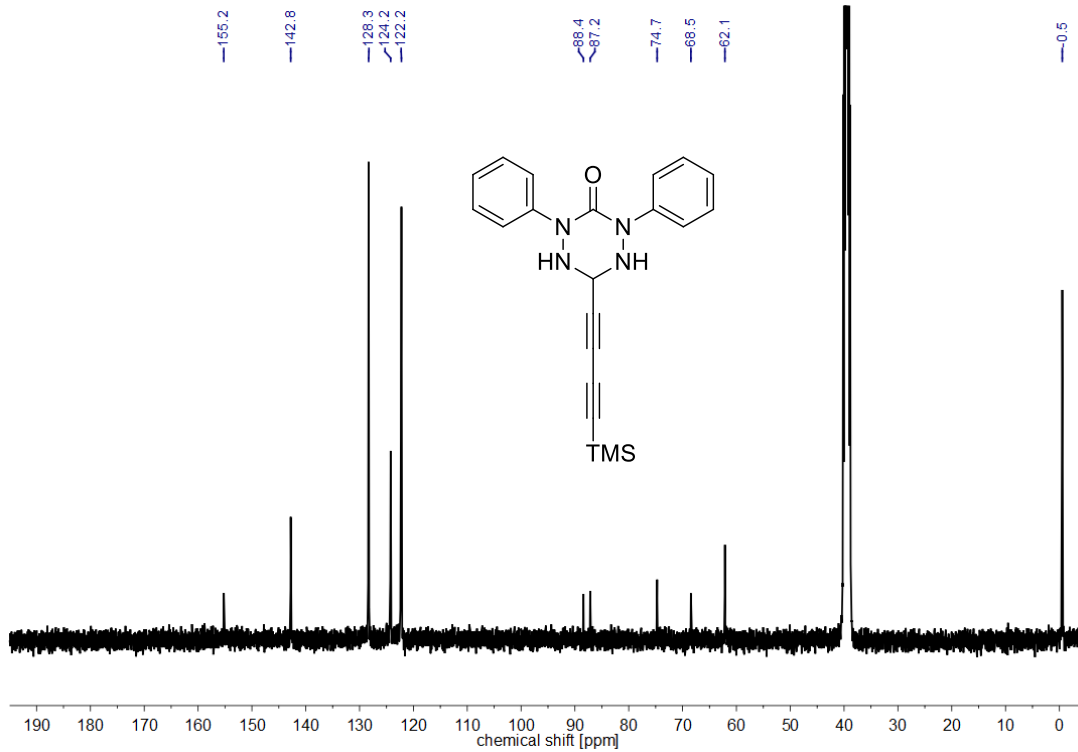
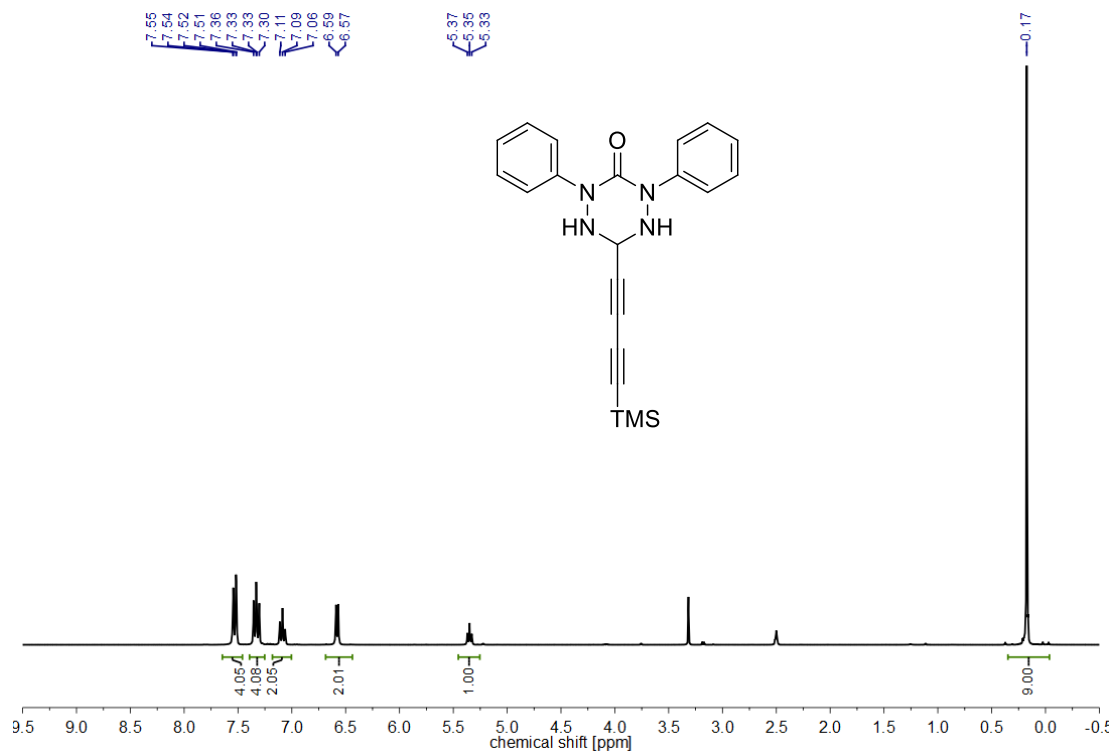
	$E_{\text{red}} / \text{V}$	$E_{\text{rox}} / \text{V}$	$E_{\text{cell}} / \text{V}$
3	-0.86	+0.56	1.42
4	-0.83	+0.58	1.41
5	-0.79	+0.59	1.38
6	-0.78	+0.61	1.39

9 ¹H and ¹³C NMR Spectra

1,5-Dihydro-2,4-diphenyl-6-trimethylsilylethynyl-1,2,4,5-tetrazinan-3(2H)-one (2a)



2,4-Diphenyl-6-((trimethylsilyl)buta-1,3-diyne-1-yl)-1,2,4,5-tetrazinan-3-one (2b)



10 References

- (1) Gottlieb, H. E.; Kotlyar, V.; Nudelman, A. *J. Org. Chem.* **1997**, *62*, 7512.
- (2) Boeckman, R. K.; Shao, P.; Mullins, J. J. *Org. Synth.* **2000**, *77*, 141.
- (3) Matuschek, D.; Eusterwiemann, S.; Stegemann, L.; Doerenkamp, C.; Wibbeling, B.; Daniliuc, C. G.; Doltsinis, N. L.; Strassert, C. A.; Eckert, H.; Studer, A. *Chem. Sci.* **2015**, *6*, 4712.
- (4) Bowling, N. P.; Burrmann, N. J.; Halter, R. J.; Hodges, J. A.; McMahon, R. J. *J. Org. Chem.* **2010**, *75*, 6382.
- (5) Rajadurai, C.; Ivanova, A.; Enkelmann, V.; Baumgarten, M. *J. Org. Chem.* **2003**, *68*, 9907.
- (6) R. W. W. Hooft, Bruker AXS, **2008**, Delft, The Netherlands.
- (7) Otwinowski, Z.; Minor, W. *Method Enzymol* **1997**, *276*, 307.
- (8) Otwinowski, Z.; Borek, D.; Majewski, W.; Minor, W. *Acta Crystallogr. A* **2003**, *59*, 228.
- (9) Sheldrick, G. M. *Acta Crystallogr. A* **1990**, *46*, 467.
- (10) XP – Interactive molecular graphics, version 5.1, Bruker AXS Inc., Madison, WI, USA, **1998**.
- (11) APEX2 (**2014**), SAINT (**2013**), SADABS (**2014**), Bruker AXS Inc., Madison, WI, USA.
- (12) Sheldrick, G. M. *Acta Crystallogr. A* **2008**, *64*, 112.
- (13) A.L. Spek, *Acta Crystallogr.* **2009**, *D65*, 148.
- (14) Eusterwiemann, S.; Matuschek, D.; Stegemann, L.; Klabunde, S.; Doerenkamp, C.; Daniliuc, C. G.; Doltsinis, N. L.; Strassert, C. A.; Eckert, H.; Studer, A. *Chimia* **2016**, *70*, 172.
- (15) Dresselhaus, T.; Eusterwiemann, S.; Matuschek, D. R.; Daniliuc, C. G.; Janka, O.; Pöttgen, R.; Neugebauer, J. *Phys. Chem. Chem. Phys.* **2016**, *18*, 28262.
- (16) Novoa, J. J.; Deumal, M.; Jornet-Somoza, J. *Chem. Soc. Rev.* **2011**, *40*, 3182.
- (17) Deumal, M.; Bearpark, M. J.; Novoa, J. J.; Robb, M. A. *J. Phys. Chem. A* **2002**, *106*, 1299.
- (18) Neese, F. *WIREs Comput. Mol. Sci.* **2012**, *2*, 73.
- (19) Adamo, C.; Barone, V. *J. Chem. Phys.* **1999**, *110*, 6158.
- (20) Zheng, J.; Xu, X.; Truhlar, D. G. *Theor. Chem. Acc.* **2011**, *128*, 295.
- (21) Bader, R. F. *Acc. Chem. Res.* **1985**, *18*, 9.
- (22) te Velde, G.; Bickelhaupt, F. M.; Baerends, E. J.; van Ginsbergen, S. J.; Fonseca Guerra, C.; Snijders, J. G.; Ziegler, T. *J. Comput. Chem.* **2001**, *22*, 931.
- (23) van Lenthe, E.; Baerends, E. J. *J. Comput. Chem.* **2003**, *24*, 1142.